Numerical homogenization by an adaptive Fourier spectral method on non-uniform grids using optimal transport

Cédric Bellis, Renaud Ferrier

To cite this version:

Cédric Bellis, Renaud Ferrier. Numerical homogenization by an adaptive Fourier spectral method on non-uniform grids using optimal transport. Computer Methods in Applied Mechanics and Engineering, 2024, 419, pp.116658. ⟨10.1016/j.cma.2023.116658⟩. ⟨hal-04211416v2⟩

HAL Id: hal-04211416
https://hal.science/hal-04211416v2

Submitted on 5 Dec 2023

Numerical homogenization by an adaptive Fourier spectral method on non-uniform grids using optimal transport

Cédric Bellis[1], Renaud Ferrier[2]

[1]Aix Marseille Univ, CNRS, Centrale Marseille, LMA, Marseille, France

[2] Mines Saint-Etienne, University of Lyon, CNRS, UMR 5307 LGF, Centre SMS, Saint-Etienne, France

Abstract

This article focuses on the computation of the solutions to periodic cell problems that arise in a number of homogenization schemes. Formulated in terms of a generic constitutive relation, encompassing the linear and non-linear cases, a model problem is intended to be discretized on a Fourier-basis and solved using a Fast Fourier Transform (FFT)-based iterative scheme. Such a spectral method, which makes use of a uniform grid and global basis functions, has inherent limitations for correctly capturing any localized features of the solution, such as singularities or discontinuities. An adaptive method is proposed here to overcome these shortcomings. It relies on the introduction of a non-homogeneous bijective mapping between the original physical domain and a computational domain, where the Fourier spectral method will be used to solve a transformed problem. This makes it possible both to discretize the original equations on a non-uniform grid, concentrating grid points where necessary to increase computational accuracy, and to maintain the use of standard FFT schemes. To compute the mapping, an approach based on optimal transport is proposed and a numerical scheme based on FFT tools is described. A number of adaptive strategies are then discussed, either based on a priori material-based considerations, or a posteriori using a preliminary solution. The properties of the transported problem in the computational domain are described and the applicability, up to minor modifications, of a number of standard iterative schemes is discussed. A set of numerical examples is included to assess the performances of the method, both in the case of linear conductivity and for a strongly non-linear elastoplastic problem, evaluating its results both qualitatively with full-field comparisons and quantitatively with error measurements relatively to the number of iterations, the discretization and the original material contrast. Overall, these results show that, for a given discretization and compared with a computation on a regular grid, a systematic gain in accuracy is obtained using the adaptive method on a non-uniform grid.

1 Introduction

1.1 Context and motivations

The macroscopic properties of heterogeneous or microstructured media can efficiently be described and computed using homogenization methods. When the media are periodic, the numerical homogenization methods based on Fourier discretizations and the use of the Fast Fourier Transform (FFT) have shown to be very efficient since the seminal work [43, 44]. Here, we refer to these approaches as Fourier spectral methods. Over the years, the latter have been successfully applied to a vast range of materials, with a variety of microstructure geometries and constitutive laws of the featured constituents. The performances of the underlying iterative algorithms have also been greatly improved to achieve faster convergence, see the review article [52]. Recently, an effort has been made to investigate quantitatively the behavior of solutions relatively to the spatial discretization and to establish convergence proofs for these numerical methods, see [2, 64, 53], as well as to develop a posteriori errors estimators [24].

In computational homogenization we deal with heterogeneous media that are often composites materials with discontinuous constitutive properties. This results in sharp material interfaces and, possibly, geometrical corners that in turn induce discontinuities or singularities in the Partial Differential Equation (PDE) solutions. The latter are notoriously difficult to capture accurately using Fourier spectral methods, which make use of uniform computational meshes or grids. As a consequence, it may be critical to adapt the computations for such configurations and solutions as a lack of accuracy in the local fields can in turn impact the accuracy of the targeted homogenized properties.

To tackle the issue of computing singular solutions some mesh adaptation strategies have been developed in the field of computational mechanics and numerical analysis, including the following:
– *h*-adaptation, i.e. mesh refinement. In the context of FFT-based computations, where the (trigonometric) basis functions are global in nature, such a strategy would be synonymous with global grid refinement, leading to a very significant, if not prohibitive, increase in computational cost. Remarkably, interpolation schemes from coarse uniform grids to finer ones have been considered in [22] to improve the performances of FFT-based computations with global refinement. Proper local refinement can however be achieved through the use of a local multigrid approach, such as this developed in [46] based on the Local Defect Correction method.
– *p*-adaptation, i.e. increase of the polynomial degree of the approximating basis functions. In the spirit of the methods investigated here, one could consider the FFT-based implementation of high-order spectral element methods, see e.g. [9].

In the present study, we turn to the so-called *r*-adaptation strategy, i.e. remeshing or relocation methods. A number of them have been developed to accurately compute solutions with localized features, for example when dealing with time-dependent or hyperbolic PDEs as well as in phase-field problems, to cite but a few examples, see e.g. [4, 10, 11, 21, 23, 30, 29, 28, 45, 54, 62, 65, 36] and the monograph [27]. Such approaches have also been employed to deal with computations in unbounded media in order to reduce the numerical errors associated with artificial domain truncations, see [58, 15, 6, 14]. When dealing with Fourier spectral methods some algorithms such as the Non-Uniform Fast Fourier Transform (NUFFT) can be used to deal with non-equispaced grids, either in space and/or frequency, see e.g. [20], but were not considered here. For analytical homogenization problems *à la* Eshelby, the use of conformal maps in infinite domains can be powerful, see [40, Chap. 8], a tool that relates to the proposed approach. Geometrical transformations also come naturally into play in the Lagrangian formulation of large-strain problems, a framework that has been employed in [34]. This tool has recently been exploited in [66] to allow for the use of a regular computational FFT grid in combination with an irregular grid of material points that better discretizes curved interfaces. Applications to problems where the mechanics of interfaces plays a critical role can be found in [67, 25].

In this context, the purpose of this article is to investigate the possible interest of the *r*-adaptation strategy as a versatile tool in computational homogenization. The overarching question in the present study can be stated as: How to improve the accuracy of a numerical solution in FFT-based computational homogenization for a fixed discretization? In other words, considering a fixed number of degrees of freedom for a microstructure discretized using an image of $N_1 \times N_2$ pixels (in 2D, or $N_1 \times N_2 \times N_3$ voxels in 3D), we will aim at achieving improved accuracy compared to a computation on a uniform grid.
To do so, our approach will be twofold:
(i) Compute a geometrical mapping that redistributes the points of a uniform computational grid according to a desired density, typically concentrating grid points in the original physical domain where a greater accuracy is required.
(ii) Transport the PDE considered from the physical domain, by now discretized on a non-uniform grid, to the computational domain where it can ultimately be solved on a uniform grid, using standard

FFT-based numerical schemes.
First, the geometrical mapping to be used amounts to a change of coordinates associated with transformation rules for differential operators. To define and compute the former, we will consider either some analytical domain transformations, which are suitable to some specific cases, or a more generic optimal transport-based numerical method. This type of strategy has already been employed in a number of studies, although in a different context, as a moving mesh or grid generation technique, see e.g. [8, 19, 55, 38, 59]. It is based on a formulation of the Monge–Kantorovich mass transfer problem, which leads to the non-linear Monge-Ampère equation. In the present work, we propose an algorithm to solve the latter, which make use of the standard toolbox of FFT-based methods. With this tool at hand, computing the geometrical mapping requires introducing some source and target point densities, using suitable user-controlled monitor functions to define the regions of the physical domain where fewer grid points are needed or, on the contrary, where they should be concentrated. A number of possible monitor functions are proposed and discussed here, based either on a priori material-based considerations, e.g. using the detection of material interfaces or geometric singularities, or an a posteriori method based on the gradient of a preliminary solution.
Second, the original PDE considered, which constitutes a generic periodic cell problem central to a number of homogenization schemes, is transported from the physical domain to the computational domain. In doing so, the geometrical mapping mixes with the original material parameters and featured sources terms, which results in a PDE of similar type but now involving a virtual constitutive relation and virtual source terms. Some properties of the transported cell problem are analyzed and the use of standard FFT-based numerical schemes is then discussed to solve it, taking into account its specificities. Focusing first on linear conductivity problems as a proof of concept, we will provide some numerical examples to illustrate the proposed adaptive method, qualitatively comparing computations on regular and adapted grids, and then providing some quantitative convergence results. Finally, as a perspective, we illustrate our approach on a non-linear elastoplastic problem.

Following the introduction of the prototypical periodic cell problem considered, we expose the geometrical mapping formalism in Section 2. The grid adaptation strategy is then presented in Sec. 3, first using analytical transformations and then a more general optimal transport-based approach. An algorithm is developed for the latter, and a number of candidate monitor functions are investigated to drive the morphing of the computational grid. The transport of the PDE considered to the computational domain is detailed and analyzed in Section 4, and the extension of standard FFT-based schemes to solve the resulting equation is discussed in Sec. 5. The overall approach is finally illustrated by a set of numerical examples in Section 6, with full-field comparisons and convergence analyses.

1.2 Problem setting

When considering a periodic medium governed by a, possibly non-linear, local constitutive relation $\mathscr{C}$, then approximating the solution to a static or dynamic governing equation using the two-scale asymptotic homogenization method [49] leads to cell problems posed on the periodic representative volume element $\Omega_P \subset \mathbb{R}^d$. These problems all have the same structure and boil down, in acoustics, electromagnetism or elasticity, to the following generic static problem, see e.g. [17]:

$$\text{Find } \boldsymbol{u} \in H^1_{\text{per}}(\Omega_P) \text{ such that } \begin{cases} \boldsymbol{\sigma}(\boldsymbol{x}) = \mathscr{C}(\boldsymbol{x}, \boldsymbol{g}_0 + \operatorname{grad} \boldsymbol{u}), \\ \operatorname{div} \boldsymbol{\sigma}(\boldsymbol{x}) + \boldsymbol{h}(\boldsymbol{x}) = \boldsymbol{0}, \\ \langle \boldsymbol{u} \rangle_{\Omega_P} = \boldsymbol{0}. \end{cases} \tag{1}$$

For any domain Ω with associated spatial variable $\boldsymbol{\zeta}$, the averaging operator $\langle \cdot \rangle_\Omega$ is defined as

$$\langle \beta \rangle_\Omega = \frac{1}{|\Omega|} \int_\Omega \beta(\boldsymbol{\zeta}) \, \mathrm{d}\boldsymbol{\zeta}. \tag{2}$$

In (1), the unknown field $\boldsymbol{u}$ belongs to the Sobolev space $H^1_{\mathrm{per}}(\Omega_P)$ of Ω_P-periodic tensor-valued fields. In addition, $\boldsymbol{g}_0$ and $\boldsymbol{h}$ are some prescribed tensor terms. Note that the zero mean condition in (1) is meant to ensure the uniqueness of the solution. To fix ideas, in conductivity (resp. elasticity) $\boldsymbol{\sigma}$ is the current (resp. stress) field. A common formulation of (1), typically occurring in first-order homogenization schemes, uses $\boldsymbol{h} = \boldsymbol{0}$ and $\boldsymbol{g}_0 = \bar{\boldsymbol{e}}$ with $\bar{\boldsymbol{e}}$ being a uniform applied macroscopic gradient (resp. strain) associated with a periodic fluctuation of the scalar potential u (resp. vector displacement field $\boldsymbol{u}$). The cell problem (1) also generalizes to higher-order asymptotic approximation schemes, making $\boldsymbol{u}$ and the loading terms $\boldsymbol{g}_0$ and $\boldsymbol{h}$ tensors of higher ranks with some suitable symmetries.

2 Geometrical mapping

2.1 Mapping of coordinates

The solution $\boldsymbol{u}$ to (1) is known to be not well-behaved in the regions where the constitutive relation $\mathscr{C}$ involves discontinuous parameters, exhibiting large gradients that make it difficult to approximate accurately on regular grids. Therefore, achieving high-accuracy with a given number of degrees of freedom requires an adapted discretization that is *non-uniform* in space. With this issue in mind, the points $\boldsymbol{x}$ in (1) are thought of as the points of a non-uniform discretization grid covering the physical domain Ω_P, see Figure 1. Noticeably, the grid in Ω_P is possibly *deformed*, i.e. it might not be a parallelogram (2D) or a parallelepiped (3D), yet it paves all of $\mathbb{R}^d$ periodically. In this context, we consider a mapping of the periodic cell Ω_P to a computational domain Ω_C, which is intended to be discretized using a *uniform* grid. Doing so, the computations on Ω_C can be performed efficiently using FFT toolboxes. To do so, we introduce an invertible and sufficiently smooth non-homogeneous transformation $\boldsymbol{\varphi}$ such that

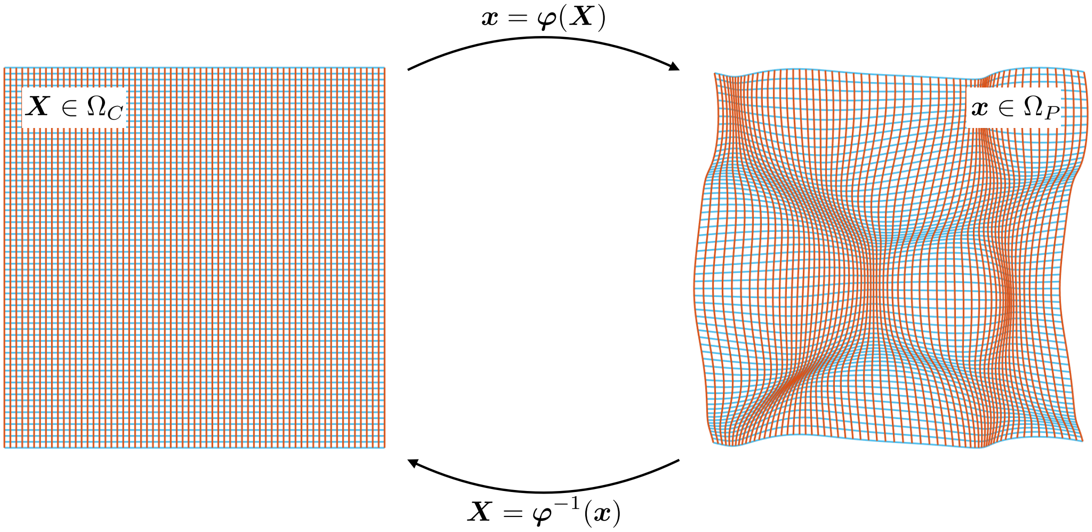

Figure 1: Coordinate mapping between the computational domain Ω_C discretized on a regular grid and the physical one Ω_P with adapted grid.

$$\boldsymbol{x} = \boldsymbol{\varphi}(\boldsymbol{X}). \tag{3}$$

The gradient of $\boldsymbol{\varphi}$ is the invertible second-order tensor $\boldsymbol{F}$, which can be represented as the Jacobian matrix of the transformation, defined locally as:

$$\boldsymbol{F}(\boldsymbol{X}) = \frac{\partial \boldsymbol{\varphi}(\boldsymbol{X})}{\partial \boldsymbol{X}} = \frac{\partial \boldsymbol{x}}{\partial \boldsymbol{X}} \qquad \text{i.e.} \qquad F_{ij} = \frac{\partial x_i}{\partial X_j} \text{ in index notation.} \tag{4}$$

In addition, the Jacobian J of the transformation is defined as

$$J(\boldsymbol{X}) = \det \boldsymbol{F}(\boldsymbol{X}).$$

We recall a useful lemma, that is a consequence of the so-called Nanson's formula for the transport of elementary surface elements:

Lemma 1. *The gradient of the transformation satisfies*

$$\mathrm{Div}\left(J\boldsymbol{F}^{-T}\right) = \boldsymbol{0},$$

where Div *is the divergence operator relatively to the variable* $\boldsymbol{X}$*, so that it holds* $\dfrac{\partial}{X_j}(JF^{-1}_{ji}) = 0$.

The mapping of fields between the two domains is achieved as follows:

Definition 1. *Let* $\boldsymbol{t}$ *be a (tensor) field on* Ω_P *then we associate it with a field* $\boldsymbol{T}$ *defined on* Ω_C *as*

$$\boldsymbol{T}(\boldsymbol{X}) = \boldsymbol{t}(\boldsymbol{\varphi}(\boldsymbol{X})) = \boldsymbol{t}(\boldsymbol{x}),$$

which defines the mapping $\boldsymbol{t} = \Phi(\boldsymbol{T})$*. In the following, lowercase (resp. uppercase) letters will be employed to denote quantities expressed on* Ω_P *(resp.* Ω_C*) according to the mapping* Φ*.*

In this context, we have the following result, see e.g. [12]:

Lemma 2. *If* $\boldsymbol{\varphi}$ *is an invertible and sufficiently smooth transformation then the mapping* Φ *is an isomorphism between the functional spaces* $W^{\ell,p}_{per}(\Omega_C)$ *and* $W^{\ell,p}_{per}(\Omega_P)$ *for any integer* $\ell \geq 0$ *and real number* $p \in [1; +\infty[$.

2.2 Transformation rules

With the purpose of transporting a given system of PDEs formulated on the physical problem Ω_P to the computational domain Ω_C we now address the transformation rules for differential operators. Considering a generic tensor field $\boldsymbol{t}$ on Ω_P, its gradient reads

$$\mathrm{grad}\,\boldsymbol{t}(\boldsymbol{x}) = \frac{\partial \boldsymbol{t}(\boldsymbol{x})}{\partial x_j} \otimes \boldsymbol{e}_j = \frac{\partial \boldsymbol{T}(\boldsymbol{X})}{\partial X_k}\frac{\partial X_k}{\partial x_j} \otimes \boldsymbol{e}_j = \frac{\partial \boldsymbol{T}(\boldsymbol{X})}{\partial X_k} F^{-1}_{kj} \otimes \boldsymbol{e}_j, \tag{5}$$

Likewise, the divergence operator transforms as

$$\mathrm{div}\,\boldsymbol{t}(\boldsymbol{x}) = \frac{\partial \boldsymbol{t}(\boldsymbol{x})}{\partial x_j} \cdot \boldsymbol{e}_j = \frac{\partial \boldsymbol{T}(\boldsymbol{X})}{\partial X_k} F^{-1}_{kj} \cdot \boldsymbol{e}_j.$$

Owing to Lemma 1, the latter term can be rewritten in divergence form, so that it holds:

$$\mathrm{div}\,\boldsymbol{t}(\boldsymbol{x}) = \frac{1}{J}\frac{\partial}{\partial X_k}\left(\boldsymbol{T}(\boldsymbol{X}) J F^{-1}_{kj}\right) \cdot \boldsymbol{e}_j. \tag{6}$$

Upon introducing the gradient operator Grad relatively to the variable $\boldsymbol{X}$, then the chain rules (5) and (6) can be put in tensor form so as to obtain the following result.

Lemma 3. *The gradient and divergence operators transform as*

$$\mathrm{grad}\,\boldsymbol{t}(\boldsymbol{x}) = \mathrm{Grad}\,\boldsymbol{T}(\boldsymbol{X}) \cdot \boldsymbol{F}^{-1} \qquad \textit{and} \qquad \mathrm{div}\,\boldsymbol{t}(\boldsymbol{x}) = \frac{1}{J}\mathrm{Div}\left(\boldsymbol{T}(\boldsymbol{X}) \cdot J\boldsymbol{F}^{-T}\right).$$

Note that we have chosen to use Lemma 1 only to transform the divergence operator into a conservative form as it corresponds to this of the problems considered hereafter. The gradient operator can also be transformed in a similar manner but it is not particularly useful to do so here.

Remark 1. *According to Definition 1, we have* $\boldsymbol{T}(\boldsymbol{X}) \cdot J\boldsymbol{F}^{-T} = \boldsymbol{t}(\boldsymbol{\varphi}(\boldsymbol{X})) \cdot J\boldsymbol{F}^{-T}$*. In the setting of finite elastic deformations the latter is sometimes referred to as the* Piola transform *of the tensor* $\boldsymbol{t}(\boldsymbol{x})$*, see [13].*

3 Grid adaptation strategies

A variety of strategies can be considered to adapt the computational grid to a specific problem through the choice of a coordinate transformation $\boldsymbol{\varphi}$. They are usually based on the introduction of a *monitor function* that will be used to relate $\boldsymbol{\varphi}$ to the material properties featured in the constitutive relation $\mathscr{C}$, i.e. the parameters of the PDE considered, or to the behavior in the physical domain of the solution $\boldsymbol{u}$ in order to concentrate grids points around singularities or discontinuities. The literature is extensive on the subject and some guidelines have been proposed to build suitable coordinate transformations, in particular using the so-called *conformity* and *equidistribution* principles, see e.g. [30, 29]. Moreover, a key issue is the problem of folded grids and mesh tangling, which can result from the distortion of the computational grid. Reference can be made to the monograph [27] for an overview of efficient strategies that have been developed in the literature, such as these based on variational approaches or mechanical models as deforming a mesh can be seen as an elasticity problem, possibly non-linear. For some specific problems, an analytical mapping of the grid can be relevant. For more general ones, we propose here a method based on optimal transport theory, whose formulation has a clear interpretation and whose implementation is both simple and guarantees the generation of a satisfactory adapted grid. These approaches are described in the next section, followed by a discussion on the choice of monitor functions.

3.1 Mapping computation

We describe here two strategies to perform the transformation of coordinates to adapt the uniform computational grid to a given material distribution or to a specific non-smooth solution. A first class of grid coordinate transformations is based on analytical mappings while a second one is based on the computation of a solution to an optimal transport problem.

3.1.1 Analytical domain transformation

In this section we focus on a prototypical example where the cell problem (1) is posed in an unbounded semi-periodic domain, such as $\Omega_P =]-\infty, +\infty[\times[-1/2, 1/2]$ with periodicity in the direction $\boldsymbol{e}_2$. This is in particular the case when one deals with the homogenization of periodic microstructured interfaces, see e.g. [37, 57]. In this context, one typically considers configurations where a set of inclusions is embedded in a homogeneous matrix and one wants to compute the solution $\boldsymbol{u}$ that is an evanescent field in the direction where the domain is unbounded, here $\boldsymbol{e}_1$. Although a dedicated method has recently been proposed in [16], a simple truncation of the computational domain is often used as the sought field $\boldsymbol{u}$ can be considered negligible away from the inclusions. In this context, domain truncation errors are unavoidable but they can be reduced if a given bounded computational domain is mapped to an extended domain where the boundaries are moved (virtually) far away from the inclusions, see [5].

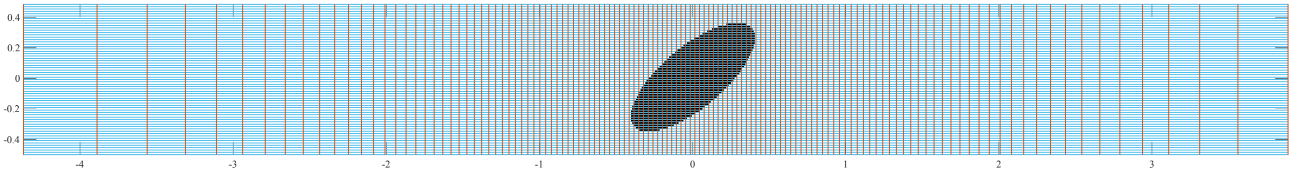

Figure 2: Non-uniform grid (red/blue) in the physical domain Ω_P obtained using an analytical mapping as in (7). Inclusion and matrix in black/white.

In this context, an analytical mapping can be employed to transform the computational domain, see [58, 15, 6, 14]. In the case where $\Omega_P =]-\infty, +\infty[\times[-1/2, 1/2]$ then, in the direction of periodicity, one can set $x_2 = X_2$ and, in the unbounded direction, define:

$$x_1 = A \tanh^{-1}(X_1/L) \tag{7}$$

with A and L being some user-chosen parameters. This is one choice among other possible ones such as $x_1 = A \tan(X_1/L)$ or $x_1 = A \sinh(X_1/L)$. The transformation is illustrated on Figure 2 where a matrix containing a tilted ellipsoidal inclusion, whose parameters are these considered in [16]. This configuration is described geometrically on a rectangular physical domain, which is discretized using a non-uniform grid generated analytically using the analytical mapping (7) of the periodic computational cell $[-1/2, 1/2] \times [-1/2, 1/2]$, itself discretized on a uniform grid of $N_1 \times N_2$ pixels, with $N_1 = 2^7 + 1$ and $N_2 = 2^6 + 1$. This allows to concentrate computational points near the inclusion while mapping non-uniformly an extended domain in the x_1-direction.

3.1.2 Optimal transport-based grid mapping

Problem formulation. In a more general geometrical setting, we adopt a strategy based on optimal transport, which provides a rational framework well-suited to the grid adaptation problem. It amounts to defining some *strictly positive* source and target densities s and t, respectively in Ω_C and Ω_P, and finding the optimal transport map $\boldsymbol{\varphi}$ between them that minimizes a given cost. In the case where the cost is defined as the discrepancy to the identity map in the L^2-norm then this problem can be interpreted as the Monge–Kantorovich mass transfer problem, see e.g. [50]. When the densities are smooth, it is well-known [7] that the sought optimal transport map $\boldsymbol{\varphi}$ can be written as the gradient of a convex potential ψ and is the unique solution to

$$t(\boldsymbol{x}(\boldsymbol{X}))J(\boldsymbol{X}) = s(\boldsymbol{X}) \quad \text{with} \quad \boldsymbol{x} = \boldsymbol{\varphi}(\boldsymbol{X}) \overset{\text{def}}{=} \operatorname{Grad}\psi(\boldsymbol{X}). \tag{8}$$

The problem (8) can be simply interpreted as this of finding the (optimal) mapping $\boldsymbol{\varphi}$ that redistributes the source density s in the computational domain Ω_C to the target density t in the physical domain Ω_P. Given the periodic boundary conditions considered, the densities and the Jacobian in (8) must satisfy some normalization conditions, see e.g. [19]. Indeed, requiring that the measure of the periodic cell is conserved through the transformation and integrating the transformation rule (8) lead to the following relations:

$$|\Omega_P| = \int_{\Omega_P} \mathrm{d}\boldsymbol{x} = \int_{\Omega_C} J(\boldsymbol{X})\,\mathrm{d}\boldsymbol{X} = |\Omega_C| \qquad \text{and} \qquad \int_{\Omega_P} t(\boldsymbol{x})\,\mathrm{d}\boldsymbol{x} = \int_{\Omega_C} s(\boldsymbol{X})\,\mathrm{d}\boldsymbol{X}. \tag{9}$$

Accordingly, the densities must also be such that

$$\int_{\Omega_C} \frac{s(\boldsymbol{X})}{t(\boldsymbol{x}(\boldsymbol{X}))}\,\mathrm{d}\boldsymbol{X} = |\Omega_P|, \tag{10}$$

which provides a normalization condition that couples s and t with the mapping $\boldsymbol{x} = \boldsymbol{\varphi}(\boldsymbol{X})$ to be found.

Using that $J(\boldsymbol{X}) = \det\left(\partial\boldsymbol{\varphi}(\boldsymbol{X})/\partial\boldsymbol{X}\right)$, the problem (8) can be directly formulated in terms of the convex potential ψ, which leads to the Monge-Ampère equation:

$$t(\operatorname{Grad}\psi(\boldsymbol{X}))\det\left(H\psi(\boldsymbol{X})\right) = s(\boldsymbol{X}), \tag{11}$$

where H is the Hessian operator, i.e. $H\psi(\boldsymbol{X}) = \operatorname{Grad}\operatorname{Grad}\psi(\boldsymbol{X})$. The formulation (11) has already been used in a number of studies as a guideline for developing a moving mesh technique, see e.g. [8, 19, 55, 38, 59]. The interest of computing the (invertible) mapping $\boldsymbol{\varphi}$ from the convex solution ψ to the Monge-Ampère equation is that it yields a transformation with a Jacobian satisfiying $J(\boldsymbol{X}) > 0$ by construction, hence preventing the deformed grid generated to be tangled. The practical computation of the solution to (11) remains a key issue. A number of methods have been proposed to do so, see [50], such as simple fixed-point iterations [3] or time-marching methods that solve some parabolic versions of (11), see [8] in connection with the grid deformation problem. Here, we have chosen to compute the solution to the non-linear elliptic equation (11) using a quasi-Newton method adapted from [35, 51].

Proposed algorithm. In the case considered of periodic boundary conditions and positive, smooth and periodic source and target densities s and t, the problem (11) is rewritten as follows [35]: define the functional f of periodic (scalar) potentials ϕ as

$$f(\phi) : \boldsymbol{X} \mapsto t(\boldsymbol{X} + \mathrm{Grad}\,\phi(\boldsymbol{X}))\det\left(\boldsymbol{I} + H\phi(\boldsymbol{X})\right) - s(\boldsymbol{X}), \tag{12}$$

and find ϕ such that

$$f(\phi) = 0 \quad \text{with} \quad \psi : \boldsymbol{X} \mapsto \frac{|\boldsymbol{X}|^2}{2} + \phi(\boldsymbol{X}) \text{ convex.} \tag{13}$$

To perform a Newton iteration on the equation (13) we linearize f as

$$\begin{aligned} f(\phi + h\tilde{\phi}) : \boldsymbol{X} \mapsto &\left\{ t(\boldsymbol{X} + \mathrm{Grad}\,\phi(\boldsymbol{X})) + h\,\mathrm{Grad}\,t(\boldsymbol{X} + \mathrm{Grad}\,\phi(\boldsymbol{X})) \cdot \mathrm{Grad}\,\tilde{\phi}(\boldsymbol{X}) \right\} \\ &\times \left\{ \det\left(\boldsymbol{I} + H\phi(\boldsymbol{X})\right)\left(1 + h\,\mathrm{tr}\left(\left(\boldsymbol{I} + H\phi(\boldsymbol{X})\right)^{-1} \cdot H\tilde{\phi}(\boldsymbol{X})\right)\right)\right\} - s(\boldsymbol{X}) + o(h). \end{aligned}$$

so that we have $f(\phi + h\tilde{\phi}) = f(\phi) + hDf(\phi) \cdot \tilde{\phi} + o(h)$ with the functional derivative being such that

$$\begin{aligned} Df(\phi) \cdot \tilde{\phi} : \boldsymbol{X} \mapsto\, & t(\boldsymbol{X} + \mathrm{Grad}\,\phi(\boldsymbol{X}))\det\left(\boldsymbol{I} + H\phi(\boldsymbol{X})\right)\mathrm{tr}\left(\left(\boldsymbol{I} + H\phi(\boldsymbol{X})\right)^{-1} \cdot H\tilde{\phi}(\boldsymbol{X})\right) \\ &+ \det\left(\boldsymbol{I} + H\phi(\boldsymbol{X})\right)\mathrm{Grad}\,t(\boldsymbol{X} + \mathrm{Grad}\,\phi(\boldsymbol{X})) \cdot \mathrm{Grad}\,\tilde{\phi}(\boldsymbol{X}). \end{aligned} \tag{14}$$

If we were to implement exact Newton iterations from the full derivative (14), then the second term would cause some difficulties. Indeed, when the target density t is defined analytically on Ω_P then its derivative can easily be computed. However, t will rather be constructed from a (preliminary) numerical solution, hence the numerical computation of its derivative will necessitate some interpolations, a process prone to errors. In this context, it has been noted in [51] and further discussed in [38] that ignoring the dependence of t on ϕ, i.e. neglecting the second term in (14), often yields satisfying results. Lastly, for the purpose of the present study, we are rather interested in an efficient grid adaptation strategy rather than in an accurate algorithm for solving the Monge-Ampère equation in itself. As a consequence, given ϕ_n, we intent to perform quasi-Newton iterations by computing instead the solution $\tilde{\phi}$ to the linearized equation $Df(\phi_n) \cdot \tilde{\phi} = -f(\phi_n)$ with the term involving $\mathrm{Grad}\,t$ being discarded in (14). After dividing by the strictly positive target density t and using (12), this leads to finding $\tilde{\phi}$ that satisfies:

$$\det\left(\boldsymbol{I} + H\phi_n(\boldsymbol{X})\right)\mathrm{tr}\left(\left(\boldsymbol{I} + H\phi_n(\boldsymbol{X})\right)^{-1} \cdot H\tilde{\phi}(\boldsymbol{X})\right) = -\det\left(\boldsymbol{I} + H\phi_n(\boldsymbol{X})\right) + \frac{s(\boldsymbol{X})}{t(\boldsymbol{X} + \mathrm{Grad}\,\phi_n(\boldsymbol{X}))}. \tag{15}$$

In [35], the equation above is discretized using a second order finite-difference scheme and inverted using the Bi-Conjugate Gradient (BiCG) algorithm. A Fourier-based discretization is rather considered in [51] but still in association with the BiCG algorithm. Yet, it should be noted that the left-hand side of the linear elliptic equation (15) can be rewritten as:

$$\det\left(\boldsymbol{I} + H\phi_n(\boldsymbol{X})\right)\mathrm{tr}\left(\left(\boldsymbol{I} + H\phi_n(\boldsymbol{X})\right)^{-1} \cdot H\tilde{\phi}(\boldsymbol{X})\right) = \mathrm{tr}\left(\mathbf{cof}\left(\boldsymbol{I} + H\phi_n(\boldsymbol{X})\right) \cdot H\tilde{\phi}(\boldsymbol{X})\right),$$

where $\mathbf{cof}(\boldsymbol{F}_n)$ is the co-factor *matrix* defined as $\mathbf{cof}(\boldsymbol{F}_n) = \det(\boldsymbol{F}_n)\boldsymbol{F}_n^{-T}$ for $\boldsymbol{F}_n = (\boldsymbol{I} + H\phi_n(\boldsymbol{X}))$, which is invertible and symmetric. As a consequence and as suggested in [50, Chap. 6], the equation (15) can be put in divergence form. Indeed, according to Lemma 1, the co-factor matrix of the gradient $\boldsymbol{F}_n = \operatorname{Grad} \boldsymbol{\varphi}_n(\boldsymbol{X})$ of any smooth vector-valued mapping $\boldsymbol{\varphi}_n(\boldsymbol{X}) = \boldsymbol{X} + \operatorname{Grad} \phi_n(\boldsymbol{X})$ is divergence-free. Therefore, we have the result that follows.

Lemma 4. *If ϕ_n is sufficiently smooth then it holds*

$$\det\left(\boldsymbol{I} + H\phi_n(\boldsymbol{X})\right) \operatorname{tr}\left(\left(\boldsymbol{I} + H\phi_n(\boldsymbol{X})\right)^{-1} \cdot H\tilde{\phi}(\boldsymbol{X})\right) = \operatorname{Div}\left(\mathbf{cof}\left(\boldsymbol{I} + H\phi_n(\boldsymbol{X})\right) \cdot \operatorname{Grad}\tilde{\phi}(\boldsymbol{X})\right).$$

This finally allows us to compute the mapping through Algorithm 1 below.

Algorithm 1. Optimal transport-based mapping computation

```
Data: Source and target densities $s$ and $t$
Initialize $\phi_0 = 0$
Iterate until convergence:
    Solve for $\tilde{\phi}$ using PCG:
        $\operatorname{Div}\left(\mathbf{cof}\left(\boldsymbol{I} + H\phi_n(\boldsymbol{X})\right) \cdot \operatorname{Grad}\tilde{\phi}(\boldsymbol{X})\right) = -\det\left(\boldsymbol{I}+H\phi_n(\boldsymbol{X})\right) + \frac{s(\boldsymbol{X})}{t(\boldsymbol{X} + \operatorname{Grad}\phi_n(\boldsymbol{X}))}$  (16)
    Compute optimal step $p$ using line search
    Define $\phi_{n+1} = \phi_n + p\,\tilde{\phi}$
Compute mapping $\boldsymbol{x} = \boldsymbol{X} + \operatorname{Grad}\phi_n(\boldsymbol{X})$
```

The equation (16) nicely exhibits a variational structure so that we can solve it using Preconditioned Conjugate Gradient (PCG) iterations, applying the differential operators Grad, Div in the Fourier space while the product with $\mathbf{cof}\left(\boldsymbol{I} + H\phi_n(\boldsymbol{X})\right)$ is computed locally in space. The chosen preconditioner is the inverse of the homogeneous Laplace operator. This preconditioner is known analytically in the Fourier space where it is diagonal and applied algebraically, see Appendix A.

Note that, to compute the solution $\tilde{\phi}$, we complement the equation (16) with a mean-free condition on $\tilde{\phi}$, which is easily imposed in the Fourier space. In addition, for (16) to be well-posed it is required that the right-hand side integrate to zero over the periodic cell Ω_C. This is indeed the case owing to the normalization conditions (9) and (10). In practice, this solvability condition may be ensured at each iteration n by renormalizing the right-hand side of (16) according to (10).

Remark 2. *Note that $\mathbf{cof}\left(\boldsymbol{I} + H\phi_n(\boldsymbol{X})\right)$ is symmetric by definition, but for (16) to be well-posed it is required that it is uniformly positive-definite as well. It is demonstrated in [35, 51] that this is the case for all n for* exact *Newton iterations. However, this cannot be guaranteed for the proposed quasi-Newton scheme and a suitable test must be used to detect if $\left(\boldsymbol{I} + H\phi_n(\boldsymbol{X})\right)$ becomes non-positive definite and stop the iterations accordingly. Another approach is to ensure ellipticity by regularizing the term $\mathbf{cof}\left(\boldsymbol{I} + H\phi_n(\boldsymbol{X})\right)$ when needed, e.g. as has been done in [63] by shifting its spectrum by a small user-chosen value, typically 10^{-5}, so that its eigenvalues remain strictly positive.*

Remark 3. *In the proposed algorithm, convergence is checked by comparing the residual to a given threshold ϵ, i.e. iterating until*

$$\frac{\|f(\phi_n)\|_{L^2(\Omega_C)}}{\|f(\phi_0)\|_{L^2(\Omega_C)}} \leq \epsilon,$$

assuming ϕ_0 is not solution, i.e. $f(\phi_0) \neq 0$. In the following, we typically set $\epsilon = 10^{-6}$ for stopping the quasi-Newton iterations and a tolerance of 10^{-1} for the inner PCG loop for solving (16). For this internal solver, this loose stopping criterion appears to be sufficient to empirically ensure convergence of the whole quasi-Newton procedure. Note that when simple CG is used (i.e. without preconditioner), *this is no longer true, and a more demanding tolerance would be needed at this step, typically* 10^{-3} *or so. Finally, a relaxation of the quasi-Newton step can also be used through a line search if necessary, as detailed in Algorithm 1.*

To conclude, let us underline that the computed transformation satisfies the following property.

Property 1. *The geometrical mapping* $\boldsymbol{x} = \boldsymbol{\varphi}_n(\boldsymbol{X})$ *computed using Algorithm 1 is such that its gradient* $\boldsymbol{F}_n$ *at the iterate* n *is given by* $\boldsymbol{F}_n = \big(\boldsymbol{I} + H\phi_n(\boldsymbol{X})\big)$*, which is symmetric.*

3.2 Monitor functions

The choice of monitor functions is a long-standing issue, see [10], which is by essence problem-dependent and through which several objectives can be sought. For example, monitor functions can be constructed a priori, based on the material distribution and the expected behavior of the solution, or a posteriori based on a computed solution, for example on a preliminary non-adapted discretization, or using an error estimator. In the following, we will not advocate for a particular choice but rather illustrate different options on the 2D microstructures of Figure 3. The optimal transport-based grid mapping method described in Section 3.1.2 will be used, with s defined as the uniform unit density while different monitor functions will be considered to define the target density t in the following. Note that setting $t = 1$ while defining the density of the source s from a given objective function does allow to deform the computational grid, but this leads to qualitatively less satisfying configurations as the density of the grid, i.e. the position of its points must rather be prescribed in the physical domain.

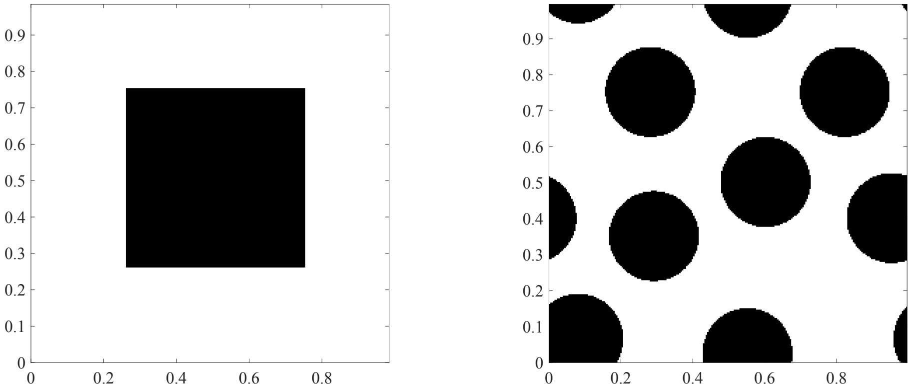

(a) Square inclusion (b) Random circular inclusions

Figure 3: Reference 2D materials distributions.

Remark 4. *As the Jacobian* J *governs the local change of surface (resp. volume in 3D) elements, then according to the definition (8) of the point densities, starting from a regular grid of pixels of surface* dS*, each of them is distorted with a local change in measure that satisfies* $ds(\boldsymbol{x}) = s(\boldsymbol{X})/t\big(\boldsymbol{x}(\boldsymbol{X})\big)\,dS$*.*

If the regular grid in Ω_C *is made of square pixels, then the previous relation can be used to get a rough estimate of the width of the deformed pixels in* Ω_P *if one ignores the distorsion of their geometry. This argument extends to 3D grids as well.*

Remark 5. *In the following, the target density will be based on some preliminary computations (see the details below). These computations are essentially performed in the physical domain* Ω_P *and, for the objective at hand, it is sufficient to perform them on a regular grid (which may be different from the computational grid ultimately used for computations in* Ω_C*). Yet, to compute the solution* ψ *to the*

Monge-Ampère equation ([11](#)) *using the proposed quasi-Newton scheme, it is necessary to interpolate the density* t *at the current location of the physical discretization points. Indeed, at a given iteration* n*, the equation* ([16](#)) *makes use of* t *at the points* $\boldsymbol{x}_n = \boldsymbol{X} + \mathrm{Grad}\,\phi_n(\boldsymbol{X})$.

Performing this interpolation accurately is necessary for the algorithm to converge well (as well as using an appropriate scaling of the density function and normalizing it as already discussed). For the examples considered below, a linear C^0 *interpolation method gave satisfying results.*

3.2.1 A priori material-based adaptation

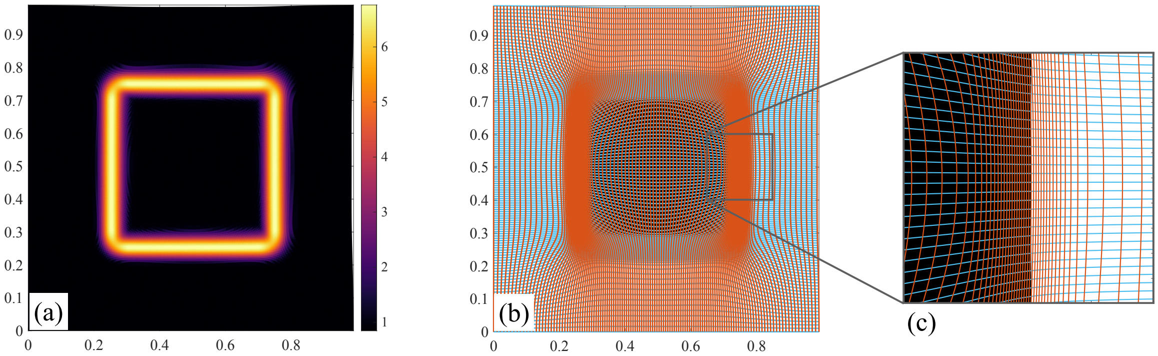

Figure 4: Grid adaptation for the square inclusion based on the detection of interfaces: (a) target density function $t(\boldsymbol{x})$, (b) adapted grid (red/blue), (c) close-up.

As the constitutive relation $\mathscr{C}$ in ([1](#)) typically features piecewise-constant material parameters, a first idea is to anticipate on the behavior of the solution $\boldsymbol{u}$ by concentrating grid points at material interfaces in the physical domain Ω_P. To do so, we propose in the linear case to simply detect the interfaces by smoothing-out the components of the material field $\boldsymbol{c}$ (using, e.g., a Gaussian filter $\mathcal{G}$) and combine them all into a single scalar image (using, e.g., the Frobenius norm $\|\cdot\|_{\mathrm{F}}$) as $\|\mathcal{G}[\boldsymbol{c}]\|_{\mathrm{F}}$. To define a target density function $\boldsymbol{x} \mapsto t(\boldsymbol{x})$ that takes large values at the (smoothed) interfaces we simply define it from the rescaled and normalized local Euclidean norm of the gradient of the previous quantity, i.e. $\|\,\mathrm{grad}\,\|\mathcal{G}[\boldsymbol{c}]\|_{\mathrm{F}}\|_2(\boldsymbol{x})$. This gradient is defined in physical space and, for the purpose considered here, it is sufficient to compute it using the Fourier spectral method on a regular grid.

This is illustrated on the examples considered in the figures [4](#) and [5](#) where a coarse grid of $N \times N$ points, with $N = 2^7 + 1$, is purposely used for a better visualization. The smoothing function $\mathcal{G}$ is a 2-D Gaussian kernel with a width of 3 pixels. The resulting target density function t is minimal in the homogeneous phases while it takes larger values in the regions neighboring the material interfaces.

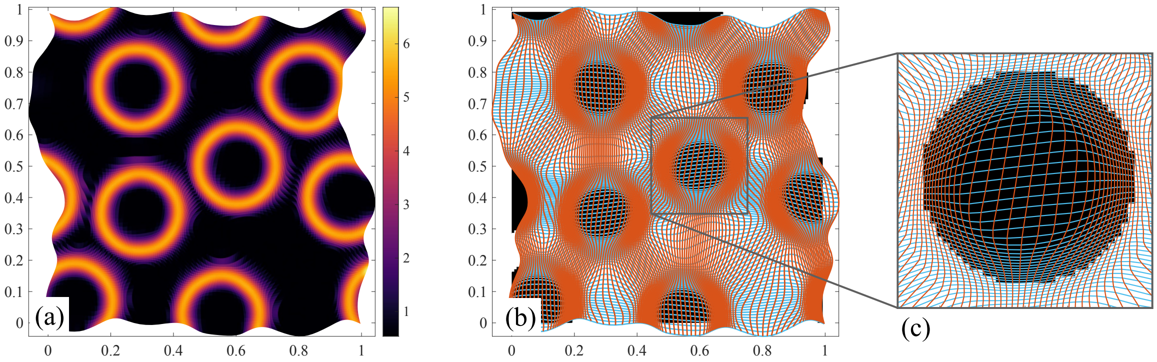

Figure 5: Grid adaptation for the random circular inclusions problem based on the detection of interfaces: (a) target density function $t(\boldsymbol{x})$, (b) adapted grid (red/blue), (c) close-up.

These regions are all the more spread out that the smoothing kernel $\mathcal{G}$ is wide, which will in turn have a direct impact on the size of the areas where the grid points are to be concentrated.

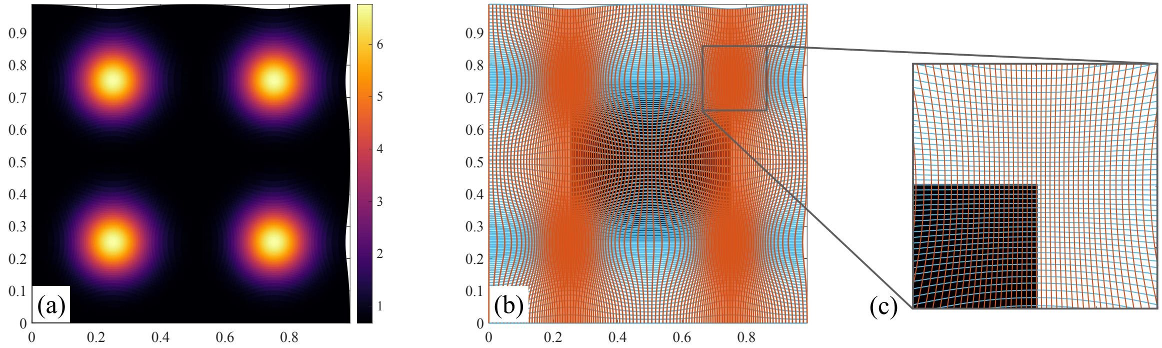

Figure 6: Grid adaptation for the square inclusion based on the location of corners: (a) analytical target density function $t(\boldsymbol{x})$, (b) adapted grid (red/blue), (c) close-up.

In the context of this a priori material-based approach of grid adaptation, alternative objectives can be considered, such as concentrating points where singularities are expected, typically around corners or where inclusions are close to touching. Simple target density functions t can be constructed either analytically or based on simple image processing techniques to do so, some examples of which are shown in the figures 6 and 7.

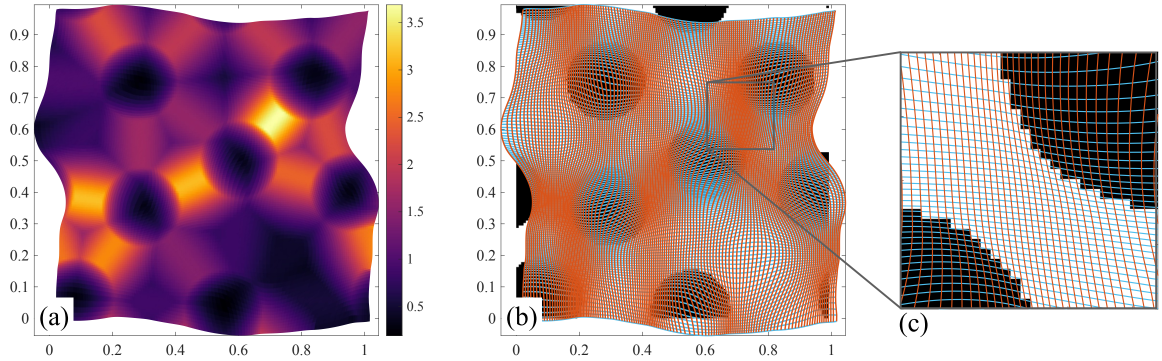

Figure 7: Grid adaptation for the random circular inclusions problem based on the mean distance to the two closest interfaces: (a) target density function $t(\boldsymbol{x})$, (b) adapted grid (red/blue), (c) close-up.

Note that, the grids generated when solving the Monge-Ampère equation using the proposed quasi-Newton iterations do remain periodic. The representative cell is deformed but it still paves the whole space periodically.

3.2.2 A posteriori solution-based adaptation

Instead of constructing the monitor function based on a priori considerations on the material properties distribution, the solution-based strategy aims at improving, a posteriori, a solution to (1) on a given discretization and given some specific source terms. There is an extensive literature on the subject, see e.g. [4, 10, 11, 21, 23, 27, 30, 29, 28, 45, 54, 62, 65]. In particular, some efficient methods have been developed based on variational approaches, dealing with the minimization of energy-like quantities. As in the previous section, we explore here simple, yet practical, ideas.

Consider first the solution $\boldsymbol{u}$ to the problem (1) with $\mathscr{C}$ linear, using $\boldsymbol{h} = \boldsymbol{0}$ and a loading arbitrarily defined as $\boldsymbol{g}_0 = (1, 0)$ for the sake of the example. The matrix and the inclusion(s) are isotropic, with conductivities 1 and $z = 10$, respectively. This solution can be computed on a preliminary regular

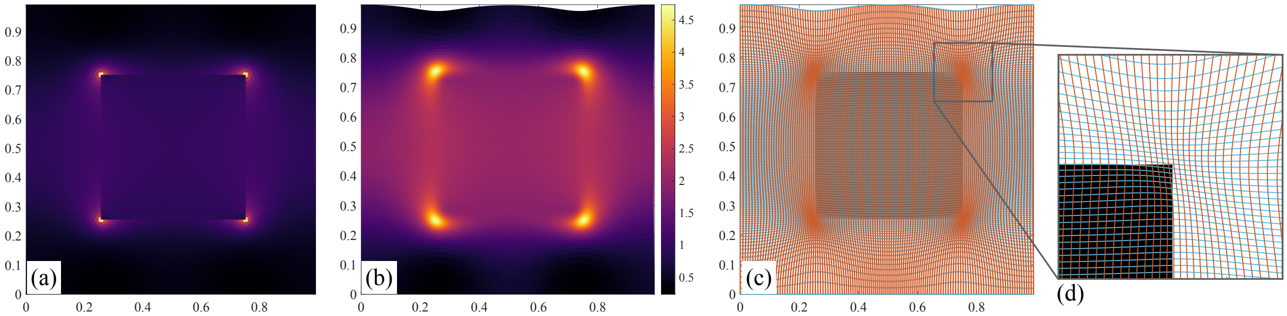

Figure 8: Grid adaptation for the square inclusion based on the computation of a preliminary solution $\boldsymbol{u}$: (a) Euclidean norm $\|\operatorname{grad}\boldsymbol{u}\|_2(\boldsymbol{x})$, (b) target density function $t(\boldsymbol{x})$, (c) adapted grid (red/blue), (d) close-up.

coarse grid in Ω_P (which, again, can be different from the computational grid ultimately used in Ω_C). This solution is relatively smooth, unlike its gradient, which can be computed using the Fourier spectral method. Then, a target density function can be computed from there by smoothing the local Euclidean norm of the gradient $\mathcal{G}[\|\operatorname{grad}\boldsymbol{u}\|_2](\boldsymbol{x})$, and applying a suitable scaling and normalization. An adapted grid obtained for each of the two examples of Figure 3 is shown in the figures 8 and 9.

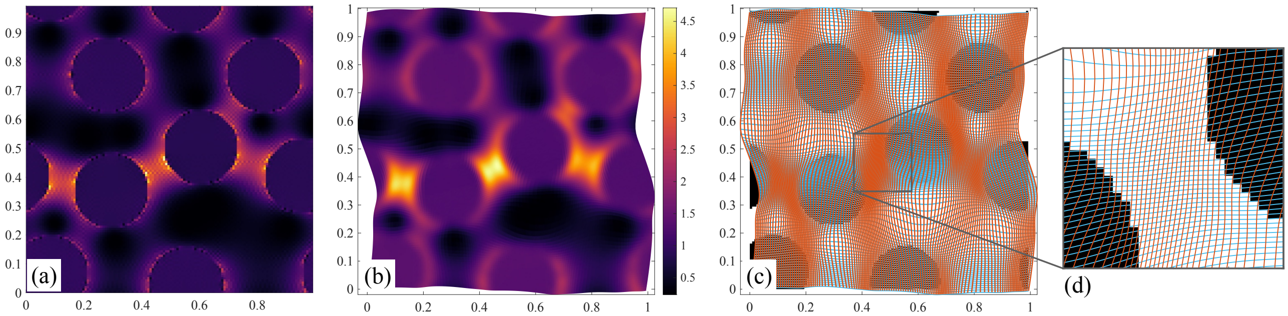

Figure 9: Grid adaptation for the random circular inclusions problem based on the computation of a preliminary solution $\boldsymbol{u}$: (a) Euclidean norm $\|\operatorname{grad}\boldsymbol{u}\|_2(\boldsymbol{x})$, (b) target density function $t(\boldsymbol{x})$, (c) adapted grid (red/blue), (d) close-up.

This approach is expected to be more adapted to the problem (1) at hand in the sense that it makes use of the actual singularities of the solution for the loading considered. Unsurprisingly, it leads to deformed grids that are similar to the ones obtained using the a priori material-based approach when the target density function was defined relatively to the singular points of the geometry (i.e. corners or regions where inclusions are close to touching). Nevertheless, only a subset of such geometrical singularities may actually be involved in the a posteriori solution-based approach as a specific loading is considered. Varying the material contrast z would obviously affect the solution $\boldsymbol{u}$ and, in turn, lead to different adapted grids. In so doing, however, we have observed that, although different, these grids are qualitatively alike, making the figures 8 and 9 relatively representative in the configurations considered. Note finally, that this a posteriori strategy readily allows for an iterative adaptive approach to be used (see Section 5.2.2). In addition, a posteriori error estimators, such as these proposed in [24] could advantageously be used at this step.

4 Computational domain formulations

Now that we have some tools to compute mappings between a uniform grid in the computational domain Ω_C and adapted ones in the physical domain Ω_P, it remains to transport the PDE considered from Ω_P to Ω_C where it will be solved numerically. This is addressed in this section, first in the generic case and then in the linear conductivity and elasticity cases where we highlight some additional properties.

4.1 Transported cell problem

Owing to Lemma 2 and to the transformation rules of Lemma 3 then the generic cell problem (1) when transported from Ω_P to Ω_C reads as:

$$\text{Find } \boldsymbol{U} \in H^1_{\text{per}}(\Omega_C) \text{ such that } \begin{cases} \boldsymbol{\Sigma}(\boldsymbol{X}) = \mathscr{C}(\boldsymbol{\varphi}(\boldsymbol{X}), \boldsymbol{G}_0 + \operatorname{Grad} \boldsymbol{U} \cdot \boldsymbol{F}^{-1}), \\ \operatorname{Div}\left(\boldsymbol{\Sigma}(\boldsymbol{X}) \cdot J(\boldsymbol{X}) \boldsymbol{F}^{-T}(\boldsymbol{X})\right) + J(\boldsymbol{X}) \boldsymbol{H}(\boldsymbol{X}) = \boldsymbol{0}, \\ \overline{\boldsymbol{U}} = \boldsymbol{0}. \end{cases} \tag{17}$$

In the problem above, the transformed mean value $\overline{\boldsymbol{U}}$ is defined as

$$\overline{\boldsymbol{U}} = \left(\int_{\Omega_C} J(\boldsymbol{X})\, \mathrm{d}\boldsymbol{X}\right)^{-1} \int_{\Omega_C} \boldsymbol{U}(\boldsymbol{X}) J(\boldsymbol{X})\, \mathrm{d}\boldsymbol{X} = \frac{\langle \boldsymbol{U} J \rangle_{\Omega_C}}{\langle J \rangle_{\Omega_C}}. \tag{18}$$

The problem (17) features the original constitutive relation $\mathscr{C}$, evaluated at the image point $\boldsymbol{x} = \boldsymbol{\varphi}(\boldsymbol{X})$, combined with the gradient of the transformation, and similarly for the equilibrium equation. In an effort to have a method that is as little intrusive as possible, it is useful to rewrite (17) in a form close to that of (1) by introducing a *virtual* constitutive equation and some *virtual* source terms. This is straightforward to do so, and the final result is stated in the form of the following property.

Property 2. *The transported cell problem is given by:*

$$\textit{Find } \boldsymbol{U} \in H^1_{\text{per}}(\Omega_C) \textit{ such that } \begin{cases} \widetilde{\boldsymbol{\Sigma}}(\boldsymbol{X}) = \widetilde{\mathscr{C}}(\boldsymbol{\varphi}(\boldsymbol{X}), \widetilde{\boldsymbol{G}}_0 + \operatorname{Grad} \boldsymbol{U}) \\ \operatorname{Div} \widetilde{\boldsymbol{\Sigma}}(\boldsymbol{X}) + \widetilde{\boldsymbol{H}}(\boldsymbol{X}) = \boldsymbol{0} \\ \overline{\boldsymbol{U}} = \boldsymbol{0}, \end{cases} \tag{19}$$

where the overall stress $\widetilde{\boldsymbol{\Sigma}}$ *is expressed in terms of the* virtual *constitutive relation* $\widetilde{\mathscr{C}}$ *defined as*

$$\widetilde{\mathscr{C}}(\boldsymbol{\varphi}(\boldsymbol{X}), \boldsymbol{E}) = \mathscr{C}(\boldsymbol{\varphi}(\boldsymbol{X}), \boldsymbol{E} \cdot \boldsymbol{F}^{-1}) \cdot J(\boldsymbol{X}) \boldsymbol{F}^{-T}(\boldsymbol{X}). \tag{20}$$

In addition, (19) *features some* virtual *source terms defined as*

$$\widetilde{\boldsymbol{G}}_0(\boldsymbol{X}) = \boldsymbol{G}_0(\boldsymbol{X}) \cdot \boldsymbol{F}(\boldsymbol{X}) \qquad \textit{and} \qquad \widetilde{\boldsymbol{H}}(\boldsymbol{X}) = J(\boldsymbol{X}) \cdot \boldsymbol{H}(\boldsymbol{X}). \tag{21}$$

The problem (19) is the one to be solved on a regular grid in Ω_C. In this form, standard tools can be employed to do so, provided that the constitutive relation and the source terms are modified to take into account the transformation of the grid. To shed light on the resulting overall behavior, we provide further details in the linear case in the next section.

Remark 6. *If Algorithm 1 were to be used to compute the geometrical mapping* $\boldsymbol{\varphi}$ *then the associated transformation gradient* $\boldsymbol{F}$ *in Property 2 would be symmetrical, see Property 1. In addition, some simplifications occur if the normalization conditions* (9) *and* (10) *are met. Nevertheless, we prefer to keep* $\boldsymbol{F}$ *and its transposed in the final formulation of the problem to make it as general as possible.*

4.2 Properties in the linear case

In the physical configurations of interest here, the constitutive relation reads in the linear case as

$$\mathscr{C}(\boldsymbol{x},\boldsymbol{e}) = \boldsymbol{c}(\boldsymbol{x})\boldsymbol{e}(\boldsymbol{x}) \tag{22}$$

where $\boldsymbol{c}$ is either a second- or fourth-order tensor-valued field, which is positive-definite, bounded above and symmetric, i.e. $\boldsymbol{c}^T = \boldsymbol{c}$. In conductivity (resp. elasticity), $\boldsymbol{c}$ is the second-order conductivity (resp. fourth-order elasticity) tensor. As such, $\boldsymbol{c}$ is everywhere diagonalizable, i.e. there exist some strictly positive scalars $\lambda_j(\boldsymbol{x})$ and tensors $\boldsymbol{k}_j(\boldsymbol{x})$, which are symmetric in the elasticity case, such that the following decomposition holds locally:

$$\boldsymbol{c}(\boldsymbol{x}) = \sum_{j=1}^{j_{\max}} \lambda_j(\boldsymbol{x})\boldsymbol{k}_j(\boldsymbol{x}) \otimes \boldsymbol{k}_j(\boldsymbol{x}), \tag{23}$$

where $j_{\max}$ depends on the dimension d and the nature of the problem considered (for conductivity problems $j_{\max} = d$ while in elasticity $j_{\max} = d(d+1)/2$). The scalars $\lambda_j(\boldsymbol{x}) > 0$ are the (possibly multiple) eigenvalues of the constitutive tensor $\boldsymbol{c}(\boldsymbol{x})$ while $\boldsymbol{k}_j(\boldsymbol{x})$ are the associated eigentensors. The eigentensors associated with distinct eigenvalues $\lambda_j(\boldsymbol{x})$ are orthogonal for the standard Euclidean scalar product. In elasticity, the relation (23) is known as the Kelvin decomposition, see [39]. In this context, one can establish the following property.

Property 3. *In the linear case, the overall stress* $\widetilde{\boldsymbol{\Sigma}}$ *entering the transported cell problem* (19) *reads as*

$$\widetilde{\boldsymbol{\Sigma}}(\boldsymbol{X}) = \widetilde{\boldsymbol{C}}(\boldsymbol{X})(\widetilde{\boldsymbol{G}}_0 + \operatorname{Grad}\boldsymbol{U}), \tag{24}$$

in terms of the virtual *linear constitutive tensor* $\widetilde{\boldsymbol{C}}$ *defined as*

$$\widetilde{\boldsymbol{C}}(\boldsymbol{X}) = \sum_{j=1}^{j_{\max}} J\Lambda_j(\boldsymbol{X})\Big(\boldsymbol{K}_j(\boldsymbol{X})\cdot\boldsymbol{F}^{-T}\Big) \otimes \Big(\boldsymbol{K}_j(\boldsymbol{X})\cdot\boldsymbol{F}^{-T}\Big),$$

using the transformation rule of Definition 1 with the associated upper-case letters notation.

Proof. Given the linear constitutive relation (22), then from the virtual constitutive equation (20) of the transported problem one can establish the following algebraic identities

$$\begin{aligned}
\boldsymbol{\Sigma}\cdot J\boldsymbol{F}^{-T} &= \Big(\boldsymbol{C}(\boldsymbol{X})(\boldsymbol{G}_0 + \operatorname{Grad}\boldsymbol{U}\cdot\boldsymbol{F}^{-1})\Big)\cdot J\boldsymbol{F}^{-T},\\
&= \Big(\Big(\boldsymbol{C}(\boldsymbol{X})\cdot\boldsymbol{F}^{-T}\Big)(\boldsymbol{G}_0\cdot\boldsymbol{F} + \operatorname{Grad}U)\Big)\cdot J\boldsymbol{F}^{-T},\\
&= \underbrace{\Big(\sum_{j=1}^{j_{\max}} J\Lambda_j(\boldsymbol{X})\Big(\boldsymbol{K}_j(\boldsymbol{X})\cdot\boldsymbol{F}^{-T}\Big)\otimes\Big(\boldsymbol{K}_j(\boldsymbol{X})\cdot\boldsymbol{F}^{-T}\Big)\Big)}_{\overset{\text{def}}{=}\widetilde{\boldsymbol{C}}(\boldsymbol{X})}\Big(\underbrace{\boldsymbol{G}_0\cdot\boldsymbol{F}}_{\overset{\text{def}}{=}\widetilde{\boldsymbol{G}}_0} + \operatorname{Grad}\boldsymbol{U}\Big).
\end{aligned} \tag{25}$$

In (25) we have made use of the notation convention associated with the mapping of Definition 1. In addition, we have also employed the Kelvin decomposition (23) where, at least in elasticity, the symmetry of the eigentensors $\boldsymbol{K}_j(\boldsymbol{X}) = \boldsymbol{k}_j(\boldsymbol{x})$ is used at the last line. ☐

In Property 3 one has defined a *virtual* local constitutive tensor $\widetilde{\boldsymbol{C}}(\boldsymbol{X})$ that combines both the actual material properties at the image point $\boldsymbol{x} = \boldsymbol{\varphi}(\boldsymbol{X})$, owing to $\Lambda_j(\boldsymbol{X}) = \lambda_j(\boldsymbol{x})$ and $\boldsymbol{K}_j(\boldsymbol{X})$, and the geometrical contribution of the grid mapping, owing to the terms $J(\boldsymbol{X})$ and $\boldsymbol{F}(\boldsymbol{X})$. In addition, as $\Lambda_j(\boldsymbol{X}) > 0$ from the original tensor $\boldsymbol{c}(\boldsymbol{x})$ being positive-definite, and since $J > 0$ with $\boldsymbol{F}$ being invertible, then one immediately obtains from Property 3 the following corollary.

Corollary 1. *The virtual constitutive tensor* $\widetilde{\boldsymbol{C}}(\boldsymbol{X})$ *is positive-definite.*

In the next two subsections we further investigate the symmetry properties of these terms in the conductivity and elasticity cases.

4.2.1 Conductivity

In the conductivity case, the unknown in (1) is a scalar potential u and $\boldsymbol{c}$ is a positive-definite and symmetric second-order tensor. As a consequence, the cell problem (19) transposed on Ω_C retains the same form as the original problem with the *virtual* second-order conductivity tensor $\widetilde{\boldsymbol{C}}$ satisfying $\widetilde{C}_{ij}(\boldsymbol{X}) = J(\boldsymbol{X})C_{pq}(\boldsymbol{X})\left(F^{-T}(\boldsymbol{X})\right)_{pi}\left(F^{-T}(\boldsymbol{X})\right)_{qj}$ as the eigentensors $\boldsymbol{K}_j(\boldsymbol{X})$ are first-order tensors. In tensor form it holds:

$$\widetilde{\boldsymbol{C}}(\boldsymbol{X}) = J(\boldsymbol{X})\boldsymbol{F}^{-1}(\boldsymbol{X}) \cdot \boldsymbol{C}(\boldsymbol{X}) \cdot \boldsymbol{F}^{-T}(\boldsymbol{X}). \tag{26}$$

In addition, if we set the source as $\boldsymbol{g}_0(\boldsymbol{x}) = \bar{\boldsymbol{e}} \in \mathbb{R}^d$ then its virtual counterpart reads

$$\widetilde{\boldsymbol{G}}_0(\boldsymbol{X}) = \boldsymbol{G}_0(\boldsymbol{X}) \cdot \boldsymbol{F}(\boldsymbol{X}) = \boldsymbol{F}^T(\boldsymbol{X}) \cdot \bar{\boldsymbol{e}}.$$

The symmetry of the original second-order conductivity tensor $\boldsymbol{c}(\boldsymbol{x})$ yields the following property.

Corollary 2. *The virtual conductivity tensor* $\widetilde{\boldsymbol{C}}$ *defined by* (26) *is symmetric, i.e.* $\widetilde{C}_{ij}(\boldsymbol{X}) = \widetilde{C}_{ji}(\boldsymbol{X})$ *holds locally.*

4.2.2 Elasticity

In conductivity, the system (19) features a virtual constitutive tensor that is symmetric so that the transported problem retains the same structure as the original one. In the elasticity case, the coordinate mapping procedure is the same but it will be seen that this yields equations with a slightly modified structure. This is well-known in the field of transformation theory, in particular when applied to cloaking [41, 47], and this question will be returned to hereafter.

In the elasticity case, the unknown in (1) is a vector-valued displacement field $\boldsymbol{U}$ and $\boldsymbol{c}$ is the fourth-order elasticity tensor with major and minor symmetries, i.e.

$$c_{ijk\ell} = c_{k\ell ij} = c_{ij\ell k} = c_{jik\ell}.$$

Therefore, the transported problem (19) is expressed in terms of the fourth-order virtual constitutive tensor $\widetilde{\boldsymbol{C}}(\boldsymbol{X})$ defined with indices as

$$\widetilde{C}_{ijk\ell}(\boldsymbol{X}) = J(\boldsymbol{X})C_{ipkq}(\boldsymbol{X})\left(F^{-T}(\boldsymbol{X})\right)_{pj}\left(F^{-T}(\boldsymbol{X})\right)_{q\ell}, \tag{27}$$

as the eigentensors $\boldsymbol{K}_j(\boldsymbol{X})$ are second-order tensors in this case. In addition, if we choose the source term as $\boldsymbol{g}_0(\boldsymbol{x}) = \bar{\boldsymbol{e}} \in \mathbb{R}^{d\times d}_{\mathrm{sym}}$ then its virtual counterpart $\widetilde{\boldsymbol{G}}_0$ is not necessarily symmetric and is given in index notation by

$$\left(\widetilde{G}_0(\boldsymbol{X})\right)_{k\ell} = \left(G_0(\boldsymbol{X})\right)_{km}\left(F(\boldsymbol{X})\right)_{m\ell} = \bar{e}_{km}\left(F(\boldsymbol{X})\right)_{m\ell}.$$

Remark 7. *For comparison with the conductivity case, it can be noted that, given the symmetries of the elasticity tensor* $\boldsymbol{C}(\boldsymbol{X}) = \boldsymbol{c}(\boldsymbol{x})$*, one has:*

$$\widetilde{C}_{ijk\ell}(\boldsymbol{X}) = J(\boldsymbol{X})\left(F^{-1}(\boldsymbol{X})\right)_{jp}C_{pikq}(\boldsymbol{X})\left(F^{-T}(\boldsymbol{X})\right)_{q\ell}.$$

Similarly, owing to the symmetry of $\bar{\boldsymbol{e}}$*, the transported source term can be rewritten as*

$$\left(\widetilde{G}_0(\boldsymbol{X})\right)_{k\ell} = \left(\boldsymbol{F}^T(\boldsymbol{X}) \cdot \bar{\boldsymbol{e}}\right)_{\ell k}.$$

Despite the apparent similarity of the transported problem (19) compared with the original problem (1), unlike the conductivity case there is a key difference in elasticity due to a lack of symmetry of the virtual elasticity tensor $\widetilde{\boldsymbol{C}}$. This is more precisely stated in the property below.

Corollary 3. *For all invertible transformation gradient $\boldsymbol{F}(\boldsymbol{X})$, the virtual elasticity tensor $\widetilde{\boldsymbol{C}}(\boldsymbol{X})$ defined by (27) has the major index symmetry, i.e. $\widetilde{C}_{ijk\ell} = \widetilde{C}_{k\ell ij}$ holds locally.*
In addition, $\widetilde{\boldsymbol{C}}(\boldsymbol{X})$ holds the minor symmetries $\widetilde{C}_{ijk\ell} = \widetilde{C}_{ij\ell k} = \widetilde{C}_{jik\ell}$ if and only if $\boldsymbol{F}(\boldsymbol{X}) = \alpha \boldsymbol{I}$ with $\alpha \in \mathbb{R}$ locally.

Proof. The major symmetry of $\widetilde{\boldsymbol{C}}$ is an immediate consequence of this of the original elasticity tensor $\boldsymbol{C}$. Indeed, one has

$$\begin{aligned}\widetilde{C}_{ijk\ell}(\boldsymbol{X}) &= J(\boldsymbol{X}) C_{ipkq}(\boldsymbol{X}) \left(F^{-1}(\boldsymbol{X})\right)_{jp} \left(F^{-1}(\boldsymbol{X})\right)_{\ell q} \\ &= J(\boldsymbol{X}) C_{kqip}(\boldsymbol{X}) \left(F^{-1}(\boldsymbol{X})\right)_{\ell q} \left(F^{-1}(\boldsymbol{X})\right)_{jp} = \widetilde{C}_{k\ell ij}(\boldsymbol{X}).\end{aligned}$$

Now, assuming that $\widetilde{\boldsymbol{C}}$ has the minor symmetries, i.e. that $\widetilde{C}_{ijk\ell}(\boldsymbol{X}) = \widetilde{C}_{ij\ell k}(\boldsymbol{X})$, entails

$$C_{ipkq}(\boldsymbol{X}) \left(F^{-1}(\boldsymbol{X})\right)_{jp} \left(F^{-1}(\boldsymbol{X})\right)_{\ell q} = C_{ip\ell q}(\boldsymbol{X}) \left(F^{-1}(\boldsymbol{X})\right)_{jp} \left(F^{-1}(\boldsymbol{X})\right)_{kq}.$$

Using that $\left(F^{-1}(\boldsymbol{X})\right)_{pj} = \left(F^{-T}(\boldsymbol{X})\right)_{jp}$ and multiplying the above equation by $\left(F^{T}(\boldsymbol{X})\right)_{jm}$ gives

$$C_{imkq}(\boldsymbol{X}) \left(F^{-1}(\boldsymbol{X})\right)_{\ell q} = C_{im\ell q}(\boldsymbol{X}) \left(F^{-1}(\boldsymbol{X})\right)_{kq}.$$

Using that $\boldsymbol{C}^{-1} : \boldsymbol{C} = \boldsymbol{I}_4^{\mathrm{sym}}$ with $\boldsymbol{I}_4^{\mathrm{sym}}$ being the symmetric fourth-order identity tensor with components $\left(I_4^{\mathrm{sym}}\right)_{ijk\ell} = \frac{1}{2}(\delta_{ik}\delta_{j\ell} + \delta_{i\ell}\delta_{jk})$, then multiplying the equation above by $\left(C^{-1}(\boldsymbol{X})\right)_{abim}$ finally leads to

$$\delta_{ak} \left(F^{-1}(\boldsymbol{X})\right)_{\ell b} + \delta_{bk} \left(F^{-1}(\boldsymbol{X})\right)_{\ell a} = \delta_{a\ell} \left(F^{-1}(\boldsymbol{X})\right)_{kb} + \delta_{b\ell} \left(F^{-1}(\boldsymbol{X})\right)_{ka}.$$

In the identity above, all the indices are independent and free with $a, b, k, \ell \in \{1, \ldots, d\}$. Now, let examine different cases:
– if $a = k$ and $b = \ell$, but $k \neq \ell$ then $\left(F^{-1}(\boldsymbol{X})\right)_{kk} = \left(F^{-1}(\boldsymbol{X})\right)_{\ell\ell}$,
– if $a = b = k \neq \ell$ then $\left(F^{-1}(\boldsymbol{X})\right)_{\ell k} = 0$,
so that one get that $\boldsymbol{F}^{-1}(\boldsymbol{X}) = \frac{1}{\alpha} \boldsymbol{I}$ with $\alpha \in \mathbb{R}$. The reciprocal holds trivially. □

As a consequence, the transported stress field defined in the computational domain Ω_C is not symmetric. This result is already known from transformation theory, see e.g. [47], which makes the problem (19) of the form of Cosserat elasticity [18]. This type of formulation is also encountered in large strain elasticity. Moreover, the unknown in this problem is now the full gradient of $\boldsymbol{U}$, rather than its symmetric part only. This will have some consequences for the numerical strategies aiming at solving the transported problem. Yet, it should be noted that the conservation of the major symmetry for $\widetilde{\boldsymbol{C}}(\boldsymbol{X})$ ensures that the bilinear form associated with the weak formulation of (19) remains symmetric (hence the corresponding stiffness matrix in a finite element formulation).

Remark 8. *A way to preserve all the symmetries of the elasticity tensor is to modify Definition 1 when transforming the unknown $\boldsymbol{u}$ to (1), by applying to it a linear gauge transformation related to $\boldsymbol{F}$, see [47, 41]. Doing so, the equation can be put in a transformation invariant form. However, it did not appear necessary for our purposes.*

5 FFT-based computations of the transported problem

5.1 Preliminary considerations

To solve the problem (19) formulated on the uniformly discretized computational domain Ω_C, then standard FFT-based approaches can be adopted, namely fixed-point or gradient-based algorithms, see [44, 31, 1, 60] and the references therein. The notable point here is that, even in the linear case if the original constitutive tensor $\boldsymbol{c}(\boldsymbol{x})$ is isotropic, then the use of the coordinate transformation $\boldsymbol{\varphi}$ is likely to produce a virtual tensor field $\widetilde{\boldsymbol{C}}(\boldsymbol{X})$ that is anisotropic. Hence, the algorithm employed to solve (19) may need to be adapted to take this into account. In particular, for the iterative methods that rely on the introduction of a homogeneous comparison medium $\boldsymbol{C}_0$, the latter has to be suitably chosen to ensure convergence in this context. Moreover, even if the original constitutive properties are piecewise-constant, if the coordinate mapping varies continuously in space (which is likely to be the case in practice), then the overall properties in the transported problem would exhibit both smooth variations and discontinuities, inherited from $\boldsymbol{\varphi}$ and $\mathscr{C}$, respectively, as already discussed. Lastly, if there are regions where the coordinate transformation $\boldsymbol{\varphi}$ induces severe distortions to the grid then the Jacobian $J(\boldsymbol{X})$ will have extreme values at these locations (as it quantifies local volumetric changes), leading thus to very large or small values of the local properties in Ω_C (in such a case, the associated virtual material would therefore exhibit high contrasts). Lastly, the Green's tensor featured in the volume integral equation on which FFT-based methods are based on must be adapted to the specific symmetries of the virtual constitutive tensor. These questions are returned to in the next sections.

5.2 Iterative schemes

Here, we describe some iterative schemes to solve the problem (19) formulated on the reference uniform grid Ω_C, in the linear case (24) first and then in the non-linear one. The linear conductivity and elasticity problems being formally of the same nature, we expose here the main ideas behind the structure of the numerical schemes needed and, without loss of generality, we set $\boldsymbol{H} = \boldsymbol{0}$. The Green's tensors to be used specifically in the conductivity and the elasticity cases will be detailed in Appendix A.

Remark 9. *The following schemes solve for* $\operatorname{Grad}\boldsymbol{U}$ *directly rather than for* $\boldsymbol{U}$ *itself. As a consequence, no use will be made of the normalization condition* $\overline{\boldsymbol{U}} = \boldsymbol{0}$ *of* (19)*. Yet, as* $\boldsymbol{U}$ *is a periodic field on* Ω_C*, its gradient is mean-free, i.e.* $\langle \operatorname{Grad}\boldsymbol{U}\rangle_{\Omega_C} = \boldsymbol{0}$*, a condition that will be used hereafter.*

5.2.1 Green's tensor and fixed-point scheme

We now describe formally the fixed-point approach for completeness. Let $\boldsymbol{C}_0$ denote a homogeneous comparison medium and define

$$\widetilde{\boldsymbol{\Sigma}}(\boldsymbol{X}) = \boldsymbol{C}_0 \operatorname{Grad}\boldsymbol{U}(\boldsymbol{X}) + \widetilde{\boldsymbol{T}}(\boldsymbol{X}) \quad \text{with} \quad \widetilde{\boldsymbol{T}}(\boldsymbol{X}) = \widetilde{\boldsymbol{C}}(\boldsymbol{X})\widetilde{\boldsymbol{G}}_0(\boldsymbol{X}) + \delta\widetilde{\boldsymbol{C}}(\boldsymbol{X}) \operatorname{Grad}\boldsymbol{U}(\boldsymbol{X}), \tag{28}$$

with $\delta\widetilde{\boldsymbol{C}}(\boldsymbol{X}) = \big(\widetilde{\boldsymbol{C}}(\boldsymbol{X}) - \boldsymbol{C}_0\big)$. Using (28) into (19), i.e. with $\widetilde{\boldsymbol{T}}$ acting as a source term, implies that $\boldsymbol{U}$ can formally be written as

$$\boldsymbol{U}(\boldsymbol{X}) = -\big[\operatorname{Div}\boldsymbol{C}_0 \operatorname{Grad}\big]^{-1} \operatorname{Div}\widetilde{\boldsymbol{T}}(\boldsymbol{X}),$$

where the inverse is to be taken on a suitable subspace, see [40]. Therefore, as $\boldsymbol{U} \in H^1_{\mathrm{per}}(\Omega_C)$, its mean-free gradient can be found through the application of the Green's operator, which is defined as follows.

Definition 2. *The periodic gradient Green's operator* $\widetilde{\mathbf{\Gamma}}_0 : L^2_{per}(\Omega_C) \to L^2_{per,0}(\Omega_C)$ *is the non-local linear operator* formally *defined as:*

$$\widetilde{\mathbf{\Gamma}}_0\, \boldsymbol{T}(\boldsymbol{X}) = \mathrm{Grad}\left[\,\mathrm{Div}\, \boldsymbol{C}_0\, \mathrm{Grad}\,\right]^{-1} \mathrm{Div}\, \boldsymbol{T}(\boldsymbol{X}), \tag{29}$$

where $L^2_{per}(\Omega_C)$ *is the space of* Ω_C*-periodic, not necessarily symmetric, tensor-valued fields that are square-integrable, and* $L^2_{per,0}(\Omega_C)$ *its subspace of zero-mean fields.*

Accordingly, substituting the expression for $\widetilde{\boldsymbol{T}}$ back into the equation for $\boldsymbol{U}$ above yields:

$$\mathrm{Grad}\, \boldsymbol{U}(\boldsymbol{X}) = -\Big[\widetilde{\mathbf{\Gamma}}_0 \Big(\widetilde{\boldsymbol{C}}\widetilde{\boldsymbol{G}}_0 + \delta\widetilde{\boldsymbol{C}}\, \mathrm{Grad}\, \boldsymbol{U}\Big)\Big](\boldsymbol{X}). \tag{30}$$

The equation (30) is then solved by the following fixed-point scheme for all point $\boldsymbol{X}$ of a uniform grid discretizing Ω_C:

$$\begin{cases} \mathrm{Grad}\, \boldsymbol{U}^{(0)}(\boldsymbol{X}) = \boldsymbol{0}, \\ \mathrm{Grad}\, \boldsymbol{U}^{(n+1)}(\boldsymbol{X}) = \mathrm{Grad}\, \boldsymbol{U}^{(n)}(\boldsymbol{X}) - \Big[\widetilde{\mathbf{\Gamma}}_0 \widetilde{\boldsymbol{C}}\Big(\widetilde{\boldsymbol{G}}_0 + \mathrm{Grad}\, \boldsymbol{U}^{(n)}\Big)\Big](\boldsymbol{X}), \end{cases} \tag{31}$$

provided that $\boldsymbol{C}_0$ has been chosen so as to ensure convergence, see [44]. Typically, assuming that $\widetilde{\boldsymbol{C}}$ would in general be anisotropic then one can choose $\boldsymbol{C}_0$ as the closest isotropic tensor that ensures convergence [42] or as an equally suitable uniform anisotropic tensor. As is well known, the larger the contrast in $\widetilde{\boldsymbol{C}}$ the larger the number of iterations required to converge. This can however be controlled by scaling and normalizing the point densities s and t featured in the Monge-Ampère equation (11).

As is common practice, when applying the iterative scheme (31), the actions of the differential operators are computed through $\widetilde{\mathbf{\Gamma}}_0$ locally in Fourier space whereas the (virtual) constitutive properties $\widetilde{\boldsymbol{C}}$ are applied locally in the (transformed) space Ω_C. The expression of the periodic gradient Green's tensor $\widetilde{\mathbf{\Gamma}}_0$ in the Fourier space will be detailed in Appendix A. It must also be noticed that the scheme (31) has been established using the following property.

Property 4. *The periodic gradient Greens's tensor* $\widetilde{\mathbf{\Gamma}}_0$ *in Definition 2 satisfies the formal projection property:*

$$\Big[\widetilde{\mathbf{\Gamma}}_0\, \boldsymbol{C}_0\, \mathrm{Grad}\, \boldsymbol{W}\Big](\boldsymbol{X}) = \mathrm{Grad}\, \boldsymbol{W}(\boldsymbol{X}) \qquad \forall \boldsymbol{W} \in H^1_{per}(\Omega_C). \tag{32}$$

The identity (32) is well-known in the standard cases involving fully symmetric constitutive properties and symmetrized gradients. It will be further discussed in Appendix A for the specific forms of the Green's tensor $\widetilde{\mathbf{\Gamma}}_0$ involved in this study.

Finally, once the converged gradient solution has been obtained in Ω_C using (31), it can be transported back to Ω_P using Lemma 3 to approximate the solution to the original problem (1).

5.2.2 Adaptive approach

When solving (31), two approaches can be adopted. Either the coordinate transformation $\boldsymbol{\varphi}$ is fixed so that $\widetilde{\boldsymbol{C}}$ and $\widetilde{\boldsymbol{G}}_0$ are given and $\boldsymbol{C}_0$ (and thus $\widetilde{\mathbf{\Gamma}}_0$) is defined once for all, or $\boldsymbol{\varphi}$ changes with the iterations (e.g. so as to adapt to the computed solution which may be singular) so the previous quantities would change accordingly. In such a case, (31) is rewritten as

$$\begin{cases} \mathrm{Grad}\, \boldsymbol{U}^{(0)}(\boldsymbol{X}) = \boldsymbol{0}, \\ \mathrm{Grad}\, \boldsymbol{U}^{(n+1)}(\boldsymbol{X}) = \mathrm{Grad}\, \boldsymbol{U}^{(n)}(\boldsymbol{X}) - \Big[\widetilde{\mathbf{\Gamma}}_0^{(m)} \widetilde{\boldsymbol{C}}^{(m)}\Big(\widetilde{\boldsymbol{G}}_0^{(m)} + \mathrm{Grad}\, \boldsymbol{U}^{(n)}\Big)\Big](\boldsymbol{X}). \end{cases} \tag{33}$$

In (33) the terms $\widetilde{\boldsymbol{C}}^{(m)}$, $\widetilde{\boldsymbol{G}}_0^{(m)}$, and the chosen reference medium $\boldsymbol{C}_0^{(m)}$ (and hence $\widetilde{\boldsymbol{\Gamma}}_0^{(m)}$) may typically be modified at the iterations m of a loop exterior to the fixed-point iterations, once convergence has been reached. They can also change with n, for example if $\boldsymbol{\varphi}$ is modified at each fixed-point iteration with $m = n$, or a subset thereof, provided that convergence can be achieved.

5.2.3 Gradient-descent algorithms

For some time already, iterative fixed-point algorithms such as (31) tend to be substituted by gradient-descent methods. The latter are based on a variational formulation equivalent to the local problem considered. As the problem (19) in the linear case (24) involves a symmetric constitutive tensor $\widetilde{\boldsymbol{C}}$ both in the conductivity and elasticity cases (i.e. with major index symmetry in the elasticity case), they can be associated with a quadratic energy functional $\mathcal{J}$ defined as

$$\mathcal{J}(\boldsymbol{E}_*) = \frac{1}{2}\Big\langle (\widetilde{\boldsymbol{G}}_0 + \boldsymbol{E}_*)\widetilde{\boldsymbol{C}}(\widetilde{\boldsymbol{G}}_0 + \boldsymbol{E}_*)\Big\rangle_{\Omega_C} \tag{34}$$

defined over the functional space

$$\mathcal{H} = \Big\{\boldsymbol{E}_* : \ \exists \boldsymbol{W} \in H^1_{\mathrm{per}}(\Omega_C) \text{ such that } \boldsymbol{E}_* = \mathrm{Grad}\, \boldsymbol{W}\Big\},$$

and with $\widetilde{\boldsymbol{G}}_0$ being given. Therefore, (19) with (24) is formally equivalent to the minimization problem

$$\mathrm{Grad}\, \boldsymbol{U} = \arg \min_{\boldsymbol{E}_* \in \mathcal{H}} \mathcal{J}(\boldsymbol{E}_*).$$

As it has been done in previous studies, see e.g. [31, 1], the gradient $\boldsymbol{\nabla}\mathcal{J}[\boldsymbol{E}_*]$ of $\mathcal{J}$ at $\boldsymbol{E}_* \in \mathcal{H}$ can be computed when $\mathcal{H}$ is endowed with the energetic scalar product defined by the symmetric reference tensor $\boldsymbol{C}_0$ as the (symmetric and positive-definite) bilinear form $(\boldsymbol{E}_*^{(1)}, \boldsymbol{E}_*^{(2)}) \mapsto \langle \boldsymbol{E}_*^{(1)}\, \boldsymbol{C}_0\, \boldsymbol{E}_*^{(2)}\rangle_{\Omega_C}$. Upon using the (major) symmetry of $\widetilde{\boldsymbol{C}}$ it can be seen that $\boldsymbol{\nabla}\mathcal{J}[\boldsymbol{E}_*]$ is solution of

$$\mathrm{Div}\,\Big(\boldsymbol{C}_0 \boldsymbol{\nabla}\mathcal{J}[\boldsymbol{E}_*](\boldsymbol{X}) - \widetilde{\boldsymbol{C}}(\boldsymbol{X})\big(\widetilde{\boldsymbol{G}}_0(\boldsymbol{X}) + \boldsymbol{E}_*(\boldsymbol{X})\big)\Big) = \boldsymbol{0}.$$

As a consequence, owing to Property 4, we finally obtain:

$$\boldsymbol{\nabla}\mathcal{J}[\boldsymbol{E}_*](\boldsymbol{X}) = \Big[\widetilde{\boldsymbol{\Gamma}}_0\, \widetilde{\boldsymbol{C}}(\widetilde{\boldsymbol{G}}_0 + \boldsymbol{E}_*)\Big](\boldsymbol{X}). \tag{35}$$

With the gradient of the energy functional $\mathcal{J}$ at hand then the transported local problem (19) in the linear case (24) can be solved efficiently using (accelerated) gradient-descent algorithms. In most of the numerical examples that follow, we will make use of the Conjugate Gradient (CG) method.

5.3 Non-linear problems

When the original constitutive relation $\mathscr{C}$ is non-linear, then computing the solution to the transported problem (19) can be done as in [44] through fixed-point iterations of the form:

$$\begin{cases} \mathrm{Grad}\, \boldsymbol{U}^{(n)}(\boldsymbol{X}) \text{ and } \widetilde{\boldsymbol{\Sigma}}^{(n)} \text{ being known,} \\ \mathrm{Grad}\, \boldsymbol{U}^{(n+1)}(\boldsymbol{X}) = \mathrm{Grad}\, \boldsymbol{U}^{(n)}(\boldsymbol{X}) - \Big[\widetilde{\boldsymbol{\Gamma}}_0\, \widetilde{\boldsymbol{\Sigma}}^{(n)}\Big](\boldsymbol{X}), \\ \widetilde{\boldsymbol{\Sigma}}^{(n+1)}(\boldsymbol{X}) = \widetilde{\mathscr{C}}\big(\boldsymbol{\varphi}(\boldsymbol{X}), \widetilde{\boldsymbol{G}}_0 + \mathrm{Grad}\, \boldsymbol{U}^{(n+1)}\big). \end{cases} \tag{36}$$

This scheme is a straightforward extension of (31) to the non-linear case. Note that gradient-based algorithms could also be used to solve (19) in non-linear cases, but we will not go into further details here.

6 Numerical examples of adaptive computations

As already discussed in Section 5.1 the virtual constitutive properties $\widetilde{\boldsymbol{C}}$ (or $\widetilde{\mathscr{C}}$) are likely to be of larger contrast compared with the original properties $\boldsymbol{C}$ (or $\mathscr{C}$), a property induced by the mapping $\boldsymbol{\varphi}$. Consequently, an iterative scheme such as these described in Section 5.2 will certainly be slower to converge than the same scheme on a given regular grid, but the overall objective is to achieve better accuracy for this discretization in the bargain. For a detailed account on iteration and discretization errors, as well as on convergence criteria, the reader is referred to [24]. In addition, there is a third type of numerical errors that are those associated with the approximation of the microstructure geometry. In practice, these errors are most of the time discarded from the analysis as they are notoriously difficult to estimate, since what can serve as an exact (possibly analytical) reference geometry is often not accessible. However, in the configurations of Figure 3 considered here, the microstructure is defined analytically. Moreover, the square inclusion problem in Fig. 3a is correctly described on a regular grid. As a consequence for this geometry, for the transformations that do not yield a grid locally orthogonal at the matrix-inclusion interface, such as in the figures 4 and 8, then the corresponding transported problems would be associated with a *geometrical* error. In this very specific case, this downside has to be weighed against the expected gain in accuracy.

These questions will be investigated in this section by comparing computations of original problems (1) on regular grids with their transported versions in Property 2 on adapted non-uniform grids. For full-field comparisons, the solutions to the transported cell problems (19) will be transported back from the computational domain Ω_C to the physical domain Ω_P. The computation of effective properties will also serve as an overall metric to assess the performances of the proposed adaptive method. For the sake of conciseness, we have chosen to present in detail only a representative subset of numerical results, leaving aside in particular the notoriously complex question of the choice of the monitor function, discussed in section 3.2, see [10] and the references therein on this matter.

6.1 Periodic microstructured interface

First, we consider the periodic interface configuration for which the linear unit cell problem is posed on the semi-infinite domain $\Omega_P =]-\infty, +\infty[\times [-1/2, 1/2]$ which we approximate using the analytical mapping of Figure 2. The matrix and the inclusion are *isotropic* with conductivities 1 and $z = 10$, respectively. The *anisotropic* virtual conductivity tensor $\widetilde{\boldsymbol{C}}(\boldsymbol{X})$ associated with the chosen analytical mapping is diagonal, with components shown in Figure 10.

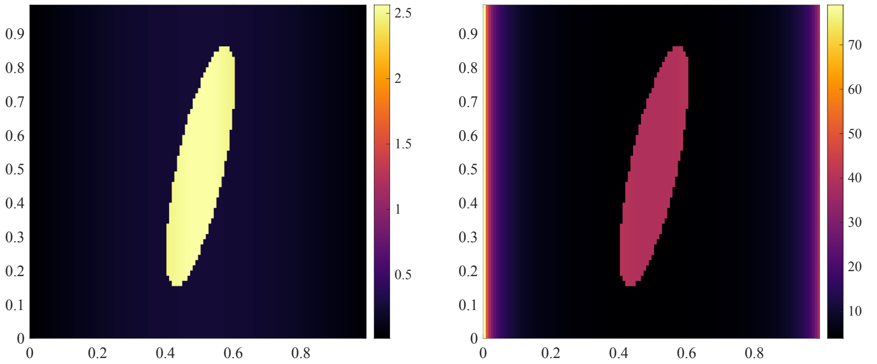

(a) $\widetilde{C}_{11}(\boldsymbol{X})$ (b) $\widetilde{C}_{22}(\boldsymbol{X})$

Figure 10: Virtual conductivity tensor in the computational domain Ω_C for the periodic interface problem and the analytical mapping of Fig. 2.

In this setting, the FFT-based computation of the transformed problem (19) are performed using fixed-point iterations on a grid of $(2^7+1)\times(2^6+1) = 8385$ pixels. Given the diagonal form of the virtual conductivity tensor, we defined the homogeneous comparison medium $\boldsymbol{C}_0$ also as anisotropic and diagonal, with components computed according to the standard rule in [44]. This departs slightly from the discussion in Section 5.2 but improved convergence.

The homogenization of the periodic interface problems is associated with a set of four effective parameters, which we refer to as B_1, B_2 and C_1, C_2, by convention with the notations in [56] and [16]. Comparison is made with both a reference Finite Element (FE) solution computed using P2 triangular elements with 80556 nodes, and a FFT-based solution computed on a regular rectangular grid of $(2^7+1)\times(2^6+1)$ pixels and whose spatial extent is identical to this of Figure 2. The results are reported in Table 1.

	Reference FE solution	FFT with regular grid	FFT with analytical mapping
B_1	-0.480	-0.469	-0.483
B_2	-0.179	-0.167	-0.174
C_1	0.179	0.167	0.174
C_2	-2.129	-2.038	-2.127

Table 1: Effective interface parameters.

First, this illustrates that the proposed adaptive Fourier spectral method on a non-uniform grid is operational. Second, it yields satisfying results regarding the computation of effective parameters. Indeed, for the case considered here, a maximum relative error of $2.5\cdot10^{-2}$ overall is obtained using the adaptive computation compared with the reference FE solution, with nearly 10 times less degrees of freedom. Meanwhile, the FFT-based computation on a regular grid yields a maximum relative error of $6.4\cdot10^{-2}$ compared to the FE solution, thereby illustrating the benefit of the proposed method.

6.2 2D periodic media and linear conductivity case

In this section we present full-field comparisons for the two cases considered in Fig. 3. The conductivity in the isotropic inclusion (or the set thereof) is set to $z = 10$ while it is equal to 1 in the matrix. The solution to the problem (1) with $\boldsymbol{h} = \boldsymbol{0}$ and an imposed macroscopic gradient $\boldsymbol{g}_0 = (1, 0)$ is computed using a relatively coarse discretization of $N\times N$ pixels with $N = 2^7+1$ for visualization, using either a conventional regular discretization or the proposed adaptive method. In each case, the CG method is employed, using the computed gradient (35) for the $\boldsymbol{C}_0$-based energetic scalar product.

Square inclusions. We investigate first the square inclusion problem of Figure 3a, in association with the mapping of Figure 6, which concentrates grid points near the inclusion corners where singularities can be expected. The use of analytical Gaussian distributions to define the target density function $t(\boldsymbol{x})$, see Fig. 6(a), allows to maintain the position of the matrix-inclusion interface and thus to better preserve the phase fraction through the transformation. Yet, the resulting virtual conductivity tensor $\widetilde{\boldsymbol{C}}(\boldsymbol{X})$ in (26) is fully anisotropic and its components are plotted in Figure 11. This is the actual conductivity tensor that is used in the transported problem (19), which is solved in Ω_C on a regular grid. Note that, while the inclusion remains a perfect square, the virtual tensor $\widetilde{\boldsymbol{C}}$ becomes fully anisotropic, with different diagonal elements and a non-zero out-of-diagonal one, and the (virtual) material contrast increases due to the local changes in the metric.

For comparison between the two types of grid, the associated first components of grad $\boldsymbol{u}$ in the physical domain Ω_P are plotted in Figure 12. A *qualitative* agreement is found between the two computed solutions. Nonetheless, despite an identical number of degrees of freedom, the corner singularities are

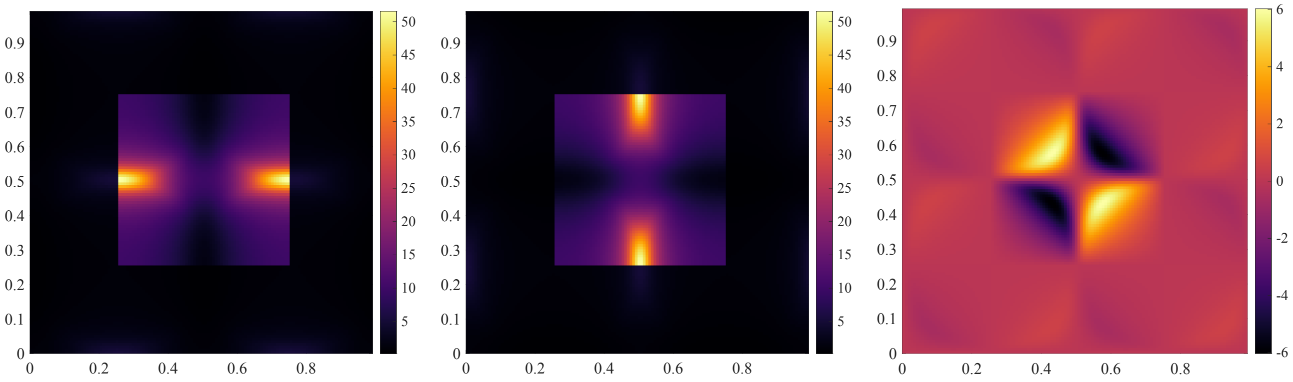

(a) $\widetilde{C}_{11}(\boldsymbol{X})$ (b) $\widetilde{C}_{22}(\boldsymbol{X})$ (c) $\widetilde{C}_{12}(\boldsymbol{X})$

Figure 11: Virtual conductivity tensor in the computational domain Ω_C for the square inclusion problem and the analytical mapping of Fig. 6.

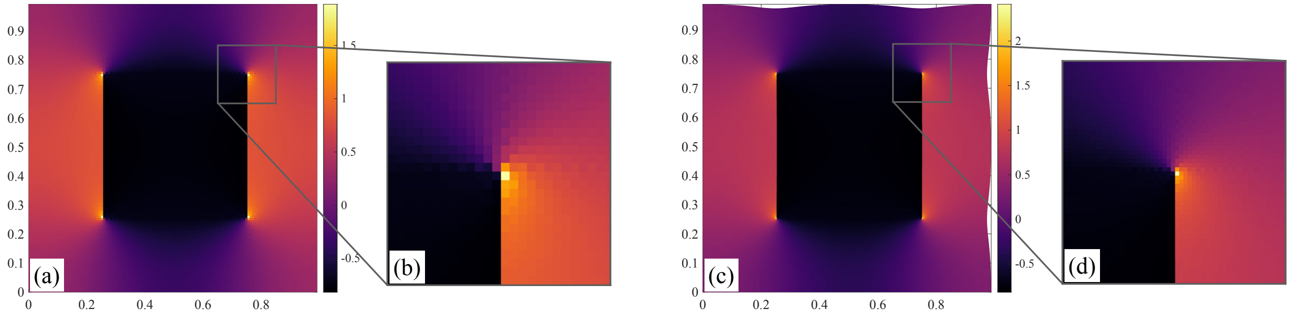

Figure 12: Square inclusion: comparison of the first component of the solution grad $\boldsymbol{u}(\boldsymbol{x})$ to (1) in Ω_P computed using (a) a regular grid and (c) the adapted grid of Fig. 6, with close-ups in (b) and (d), respectively.

better resolved using the adapted computational grid in Fig. 12(c-d). Quantitative comparisons can be found in Section 6.3.

Random circular inclusions. The geometry of the random circular inclusions in Figure 3b is now considered. An adapted grid is computed using the solution-based approach that results in Fig. 9. Doing so, grid points are concentrated in the regions where a preliminary solution computed on a regular grid exhibits strong gradients. The components of the resulting virtual conductivity tensor $\widetilde{\boldsymbol{C}}(\boldsymbol{X})$ are shown in Figure 13. As in the previous case, full anisotropy and an increase in the (virtual) material contrast are once again obtained, but here the inclusions are also distorted in the computational domain Ω_C due to the heterogeneity of the mapping.

The solution to (1) is then computed, both on a regular grid in Fig. 14(a-b), and on the adapted grid in Fig. 14(c-d). While these two simulations are comparable for this configuration as well, the adapted computation is *qualitatively* more satisfying, with a solution being smoother than the one computed on the regular grid at the same discretization, and with discontinuities being better captured. Quantitative comparisons and convergence analysis are investigated in the next section.

6.3 Convergence results

In this section, we investigate more quantitatively the effects of using the adaptive grid to compute the solution of the problem considered and, in the end, to compute homogenized parameters. As was done in [2] and [24], we distinguish between the iteration error associated with the behavior of

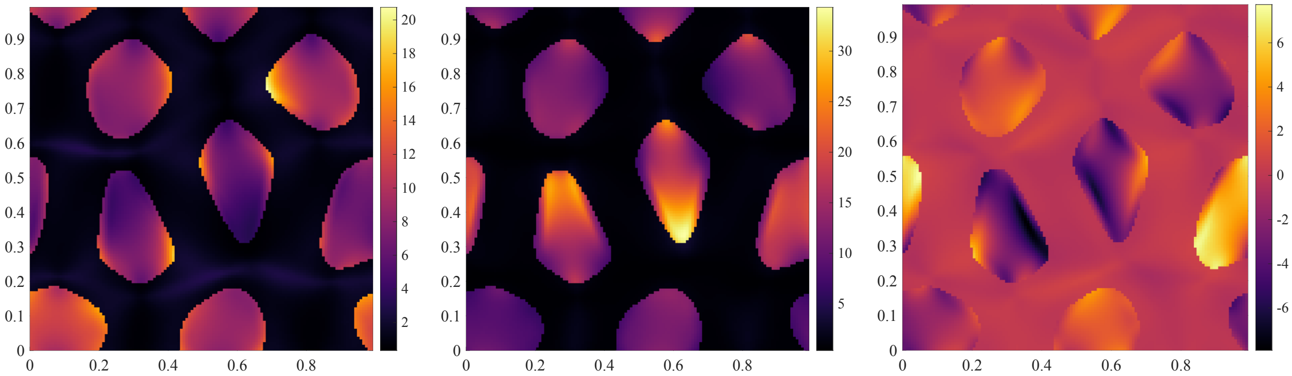

(a) $\widetilde{C}_{11}(\boldsymbol{X})$ (b) $\widetilde{C}_{22}(\boldsymbol{X})$ (c) $\widetilde{C}_{12}(\boldsymbol{X})$

Figure 13: Virtual conductivity tensor in the computational domain Ω_C for the random circular inclusions problem and the solution-based mapping of Fig. 9.

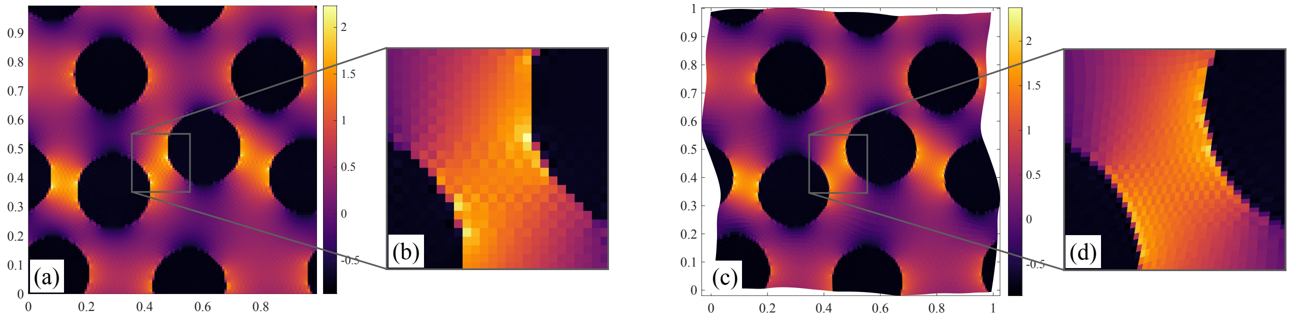

Figure 14: Random circular inclusions: comparison of the first component of the solution grad $\boldsymbol{u}(\boldsymbol{x})$ to (1) in Ω_P computed using (a) a regular grid and (c) the adapted grid of Fig. 9, with close-ups in (b) and (d), respectively.

the employed iterative scheme, see Section 5.2, and the discretization error. The results that follow correspond to the computations just described in Section 6.2. Finally, we also investigate the influence of the original material contrast on the accuracy of the proposed method. For reference, we show in the figures 15 and 16 the grids generated so far.

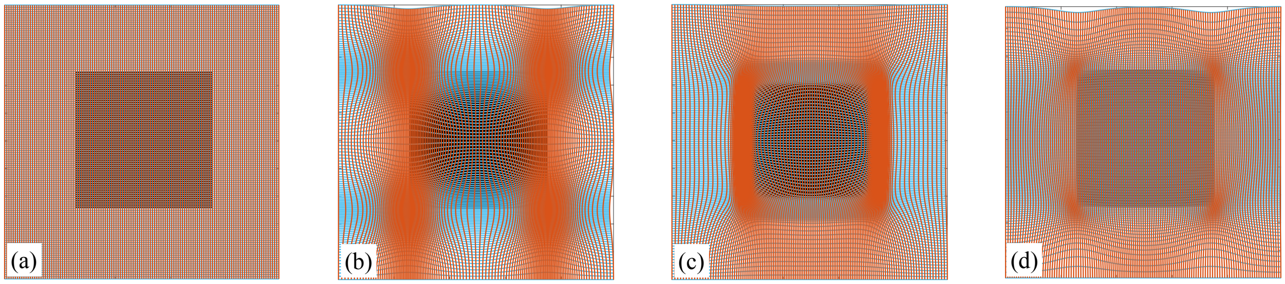

Figure 15: Grids generated in the square inclusion case: (a) uniform grid, and adapted grids based on (b) location of corners, (c) detection of interfaces, (d) preliminary solution.

6.3.1 Iteration error

First, we quantify the convergence behavior of different solution methods for solving the problem at hand. In the figures 17 and 18, the iteration error is plotted as a function of the iteration number n for

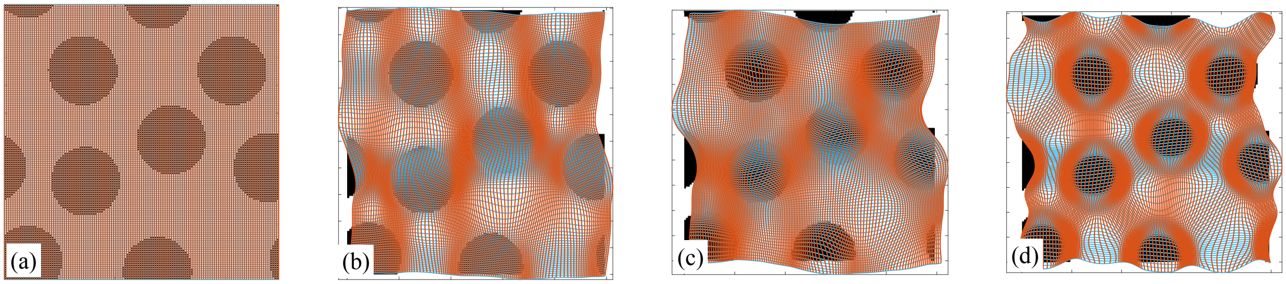

Figure 16: Grids generated in the random circular inclusions case: (a) uniform grid, and adapted grids based on (b) preliminary solution, (c) distance to closest inclusion, (d) detection of interfaces.

computations performed either on a regular grid or on an adapted one. The material contrast is set to $z = 10$ and the discretization corresponds to $N = 2^7 + 1$. Two iterative schemes are confronted, namely fixed-point iterations and the Conjugate Gradient (CG) method. In accordance with the discussion in [1], the iteration errors associated with these schemes are computed using the $\boldsymbol{C}_0$-weighted energetic norm on Ω_C of the gradient (35). These errors are normalized relatively to the loading and the stopping criterion is set to $\epsilon = 10^{-6}$. This allows iteration errors to be directly compared between the different methods. We have also included the iteration error associated with the quasi-Newton steps for solving the Monge-Ampère equation using Algorithm 1, which is used to produce the adapted grid.

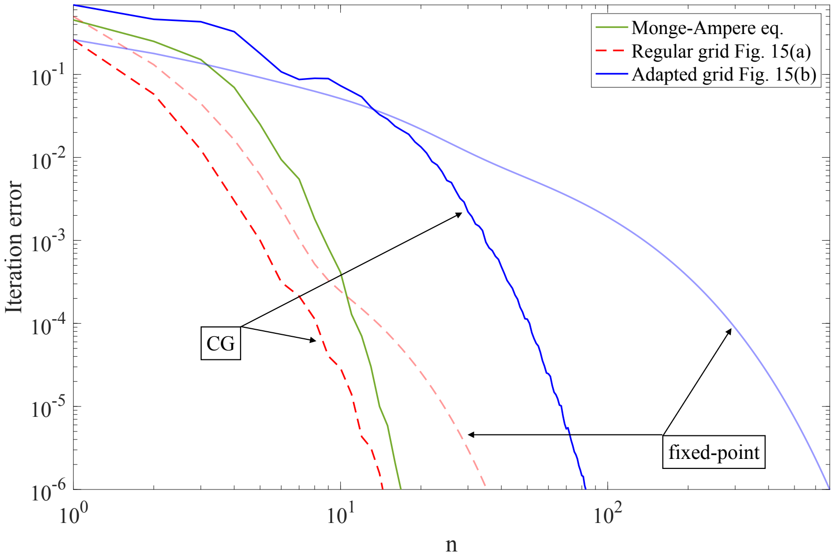

Figure 17: Square inclusion: comparison of the iteration errors in solving the PDE considered using a regular grid, Fig. 15(a), or the adapted grid of Fig. 15(b), as functions of the iteration number n (in log-log scale). The corresponding fields computed using CG are shown in Fig. 12.

The convergence behavior in the square inclusion case is highlighted in Figure 17 and this of the random circular inclusions configuration in Figure 18. As already discussed, the adaptive method solves the transported problem (19) that features a virtual material with a contrast larger than in the original problem (1). As an expected consequence, the computations performed on adapted grids take more iterations to converge. In this context, the use of an efficient gradient-based algorithm such as the CG method allows to recover satisfying performances. Note that this corresponds to the computations in Section 6.2. The additional iteration cost must be put in balance with the expected gain in accuracy that can be achieved using the proposed method, which will be quantified in the next paragraph. Note finally that, for the configurations considered, the iteration error associated with the quasi-Newton steps for solving the Monge-Ampère equation (11) is comparable to or less than this of the problem at hand itself, given that each of them only requires few inner PCG iterations with the tolerance $\epsilon = 10^{-1}$ considered, see Remark 3.

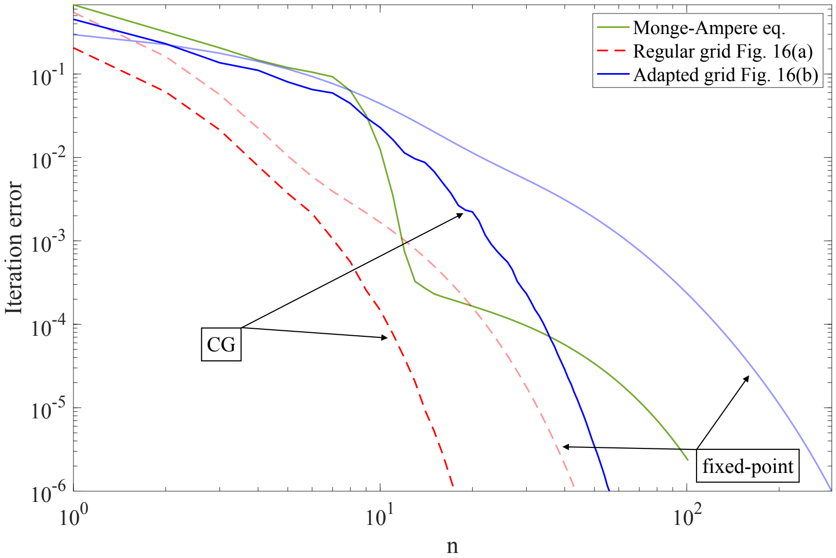

Figure 18: Random circular inclusions: comparison of the iteration errors in solving the PDE considered using a regular grid, Fig. 16(a), or the adapted grid of Fig. 16(b), as functions of the iteration number n (in log-log scale). The corresponding fields computed using CG are shown in Fig. 14.

6.3.2 Discretization error

In this section we investigate the convergence properties of the adaptive computations relatively to the discretization parameter N, the 2D computational grid being of $N \times N$ pixels. The material contrast is set to $z = 10$ and the CG method is used for these computations. We use the effective parameters as quantitative metrics to assess the performance of the proposed method. To compute the effective properties, we make use of their energetic definition, which has been proven to converge faster than the field-based version using the iterative schemes described in Section 5.2, see [2, Section 4.2]. To do so, consider the effective energy W_{eff} defined as

$$W_{\text{eff}}(\boldsymbol{g}_0) = \min_{\boldsymbol{e}_* = \operatorname{grad} \boldsymbol{w}} \langle w(\boldsymbol{x}, \boldsymbol{g}_0 + \boldsymbol{e}_*) \rangle_{\Omega_P} \tag{37}$$

in terms of the local energy density w associated with the problem (1) considered. For the adaptive computation, the averaged energy in the equation above is directly computed in the computational domain Ω_C using the transformation rules:

$$\begin{aligned} \langle w(\boldsymbol{x}, \boldsymbol{g}_0 + \operatorname{grad} \boldsymbol{w}) \rangle_{\Omega_P} &= \frac{1}{|\Omega_P|} \int_{\Omega_P} w(\boldsymbol{x}, \boldsymbol{g}_0 + \operatorname{grad} \boldsymbol{w}) \, \mathrm{d}\boldsymbol{x} \\ &= \frac{1}{|\Omega_P|} \int_{\Omega_C} w(\boldsymbol{\varphi}(\boldsymbol{X}), \boldsymbol{G}_0 + \operatorname{Grad} \boldsymbol{W} \cdot \boldsymbol{F}^{-1}) J(\boldsymbol{X}) \, \mathrm{d}\boldsymbol{X}. \end{aligned} \tag{38}$$

From (37) and (38) one can then extract some effective parameters depending on the choice of the applied macroscopic gradient $\boldsymbol{g}_0$. It is worth noting that, as is standard practice in FFT-based methods, the averaging operator $\langle \cdot \rangle_{\Omega_C}$ on the computational domain is computed using a pixel-wise summation on the associated regular FFT grid, which amounts in a trapezoidal quadrature rule [2].

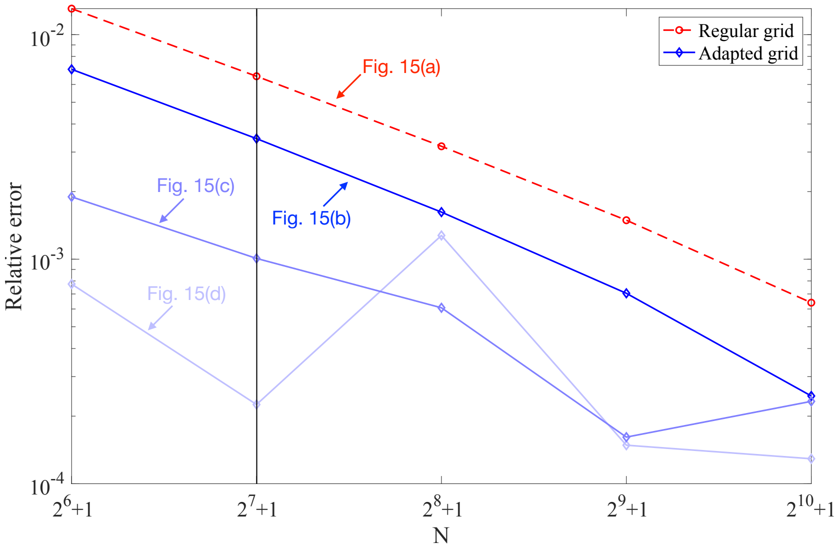

Figure 19: Square inclusion: comparison of the relative errors on the effective parameter computed using a regular grid, Fig. 15(a) and adapted ones, Fig. 15(b,c,d), as functions of the discretization parameter N (horizontal axis is in log base 2 scale). For the grids (a,b) and $N = 2^7 + 1$, see fields comparison in Fig. 12.

For the square inclusion configuration of Figure 3a, the effective parameter is known analytically, see [48]. Yet, as we have chosen to work with discretization parameters N that are odd for parity reasons in the FFT-based setting, we rather use a computation on a *regular* and sufficiently fine grid, with $N = 2^{12} + 1$, as a reference for the evaluation of numerical errors. On Figure 19, we compare the relative errors in the effective parameter associated with a macroscopic gradient $\boldsymbol{g}_0 = (1, 0)$, for computations performed on regular grids and on ones that have been adapted using the analytical mapping of Figure 6 already discussed (dark blue curve). Therefore, the case $N = 2^7 + 1$ corresponds to the computations in Section 6.2. While convergence is observed as expected for both approaches, it is remarkable here that the accuracy obtained using the proposed adaptive method at a given discretization N is comparable to the one obtained on a regular grid twice as fine, i.e. with discretization $2N$. This must be put in relation with the grid density considered in the adaptive computation (Fig. 6) where the highest value allows for a reduction of the pixel size by slightly more than two in the corner regions. This confirms the interest of the proposed approach for improving the accuracy for a given number of degrees of freedom. For completeness, we have also included the relative errors associated with the other adapted grids considered in the sections 3.2.1 and 3.2.2, see grids in Fig. 15(c,d) and light blue curves. Better accuracies are also obtained for these other grid adaptation strategies.

A convergence analysis relatively to the discretization parameter is also performed in the random circular inclusions case. Here again, errors are computed relatively to a simulation on a regular grid with $N = 2^{12} + 1$ pixels. The obtained results are synthesized in Figure 20 where, for the geometry considered, the adaptive method is deployed using the solution-based approach that leads to Figure 9 (dark blue curve) and which has been investigated previously. For this mapping, a systematic gain in accuracy is highlighted in Fig. 20 using the adapted grid compared to the regular one. While the improvement of the relative error on the effective parameter is slightly less than in the square inclusion case studied previously, it nonetheless corresponds here to a reduction between 13.5% to 48.6% for the discretizations considered, making the proposed approach interesting to improve the overall quality of the simulation. For completeness, the convergence behavior has also been quantified for the other mappings of the sections 3.2.1 and 3.2.2, see grids in Fig. 16(c,d) and light blue curves. In such cases, precision gains are nearly systematic and sometimes quite significant. Note that, in the cases

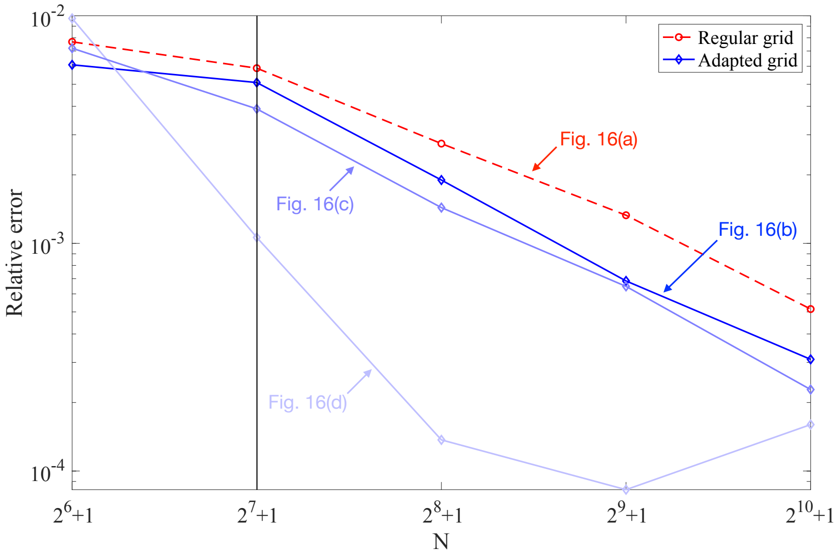

Figure 20: Random circular inclusions: comparison of the relative errors on the effective parameter computed using a regular grid, Fig. 16(a) and adapted ones, Fig. 16(b,c,d), as functions of the discretization parameter N (horizontal axis is in log base 2 scale). For the grids (a,b) and $N = 2^7 + 1$ see fields comparison in Fig. 14.

of Fig. 16(b) and (c) with $N = 2^{10} + 1$, the tolerance for the inner PCG loop had to be increased to compute the associated adapted grids, see Remark 3.

Finally, let us remark that in the figures 19 and 20 the gain in accuracy as a function of the discretization is not always monotonic for the different mappings considered. This could be due to the fact that the grid adaptation has been automatized to produce theses graphs, which could sometimes lead to suboptimal results. While these figures highlight the overall satisfying behavior of the proposed approach, the adaptive solution method must by essence be fine-tuned to a given configuration of interest to get the best performances.

6.3.3 Effect of the material contrast

Finally, we investigate here the effect of the original material contrast in the accuracy of the proposed adaptive method. Comparisons are made in this section between computations on regular and adapted grids, with a fixed discretization of $N = 2^7 + 1$ and using the CG method. The conductivity contrast z in the inclusion(s) is varied in the range $[10^{-3}, 10^3]$.

Relative error on the effective energy. The error associated with each contrast and each grid is computed relatively to a reference computation on a regular grid with $N = 2^{12} + 1$, and shown in the figures 21 and 22. First, in the square inclusion configuration in Figure 21, the error associated with the analytical mapping of Figure 6 is shown as a dark blue curve, so that the case $z = 10$ corresponds to the computations in Section 6.2 and to the errors obtained for $N = 2^7 + 1$ in Fig. 19. We observe a constant improvement in accuracy over the entire contrast range investigated. The results associated with the other mappings are also shown, see grids in Fig. 15(c,d) and light blue curves. In these cases, the evolution of the improvement is less monotonic but it is significant and particularly good in the case of the refinement at the matrix-inclusion interface, see Fig. 15(c). Similarly to the results of the previous section, optimizing the adaptive computation to a specific configuration might improve the overall performance behavior.

The random circular inclusion case is investigated in Figure 22, again with the dark blue curve corresponding to the solution-based strategy, which lead to Fig. 9. Therefore, when $z = 10$, compar-

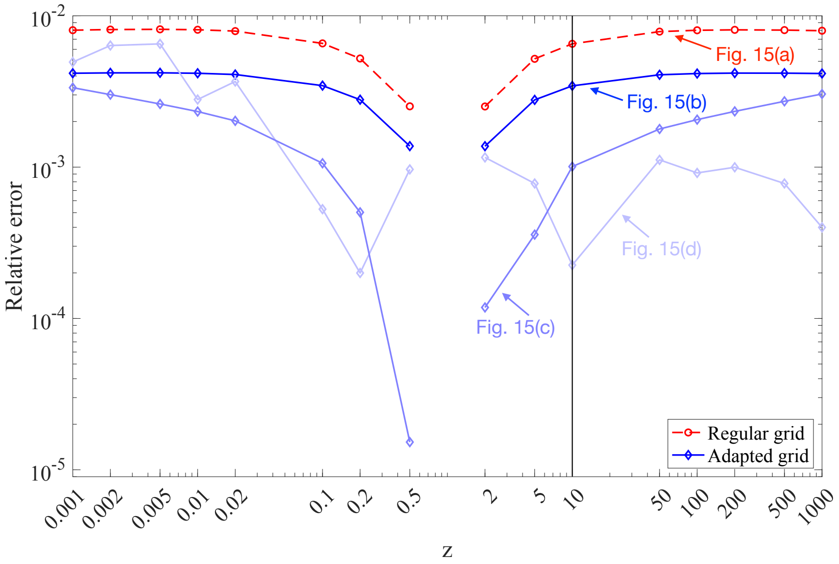

Figure 21: Square inclusion: comparison of the relative errors on the effective parameter computed using a regular grid, Fig. 15(a), and adapted ones, Fig. 15 (b,c,d), as functions of the material contrast z (in log-log scale). For the grids (a,b) and $z = 10$, see fields comparison in Fig. 12.

isons can be made with the results in Section 6.2 and in Figure 20 for $N = 2^7 + 1$. The errors for the other grid adaptation strategies are also shown, i.e. Fig. 16(c,d) and light blue curves. Overall, a constant improvement in accuracy is obtained as a function of the contrast for the different adaptive grids considered. For this configuration as well, refining at the matrix-inclusions interfaces leads to the best results, see Fig. 16(d).

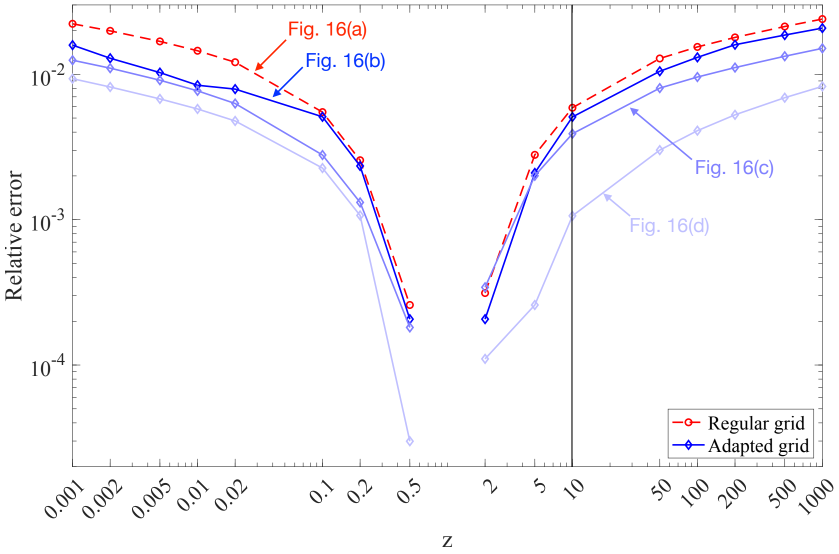

Figure 22: Random circular inclusions: comparison of the relative errors on the effective parameter computed using a regular grid, Fig. 16(a), and adapted ones, Fig. 16(b,c,d), as functions of the material contrast z (in log-log scale). For the grids (a,b) and $z = 10$, see fields comparison in Fig. 14.

Iteration number ratio. As already discussed and quantified in Section 6.3.1, the transported problem (19) exhibits a contrast in the virtual constitutive properties that is increased compared to

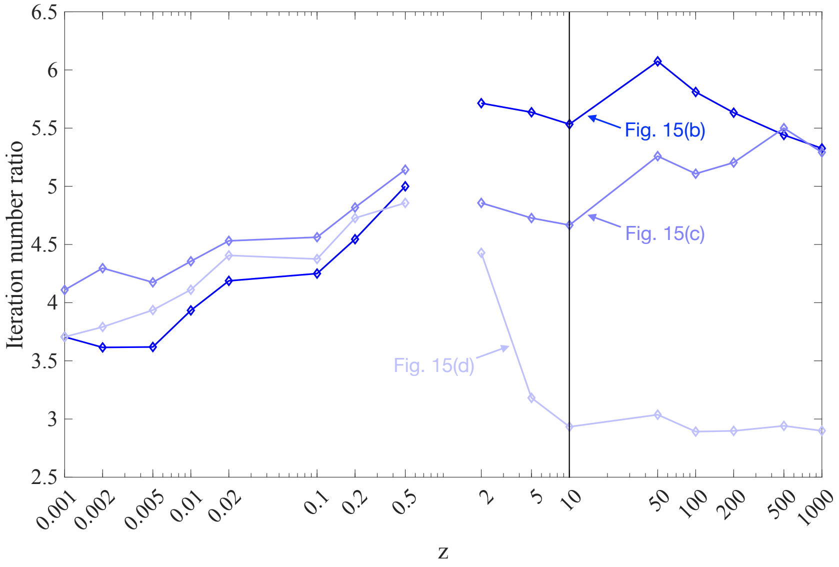

Figure 23: Square inclusion: comparison of the iteration number ratios, relatively to computations on a regular grid, Fig. 15(a), for computations on the adapted grids of Fig. 15 (b,c,d), as functions of the material contrast z (in log-log scale). For the grid (b) and $z = 10$ see Fig. 17.

the actual material contrast due to the mapping. Thus, computations on the adapted grids would take more iterations to converge. Therefore, for completeness, we provide in the figures 23 and 24 the ratio of the number of iterations at convergence for the adapted grids, relatively to a computation on a regular grid, when the original material contrast z is varied. Three observations can be made from these graphs: (i) For a given grid adaptation strategy, the iteration number ratio does not vary significantly with the original material contrast. Indeed, in the two extreme cases $z = 10^{-3}$ and 10^3 for example, the iteration number ratio is of the same order of magnitude than in the moderate contrast case, say $z = 2$. (ii) For the larger contrasts $z \gg 1$, the number of iterations tends to stabilize. This is

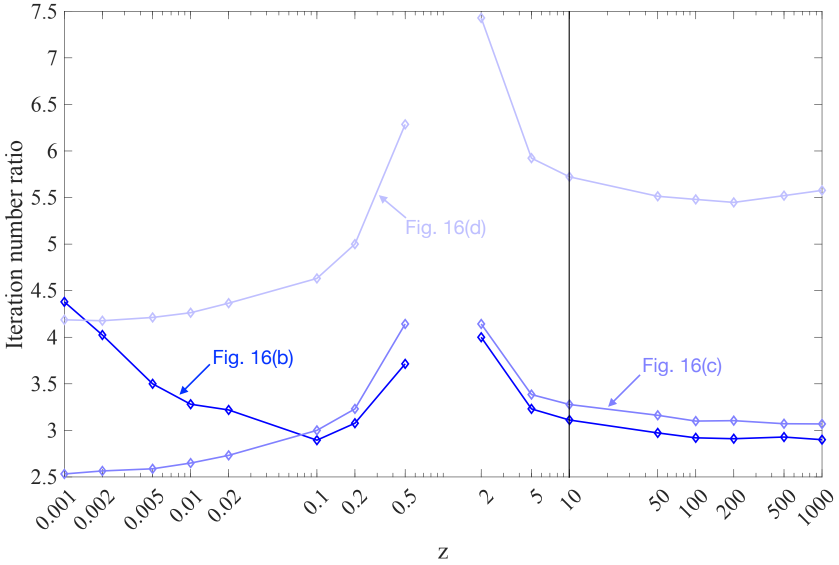

Figure 24: Random circular inclusions: comparison of the iteration number ratios, relatively to computations on a regular grid, Fig. 16(a), for computations on the adapted grids of Fig. 16 (b,c,d), as functions of the material contrast z (in log-log scale). For the grid (b) and $z = 10$ see Fig. 18.

understandable, as the relative impact of the mapping on the virtual constituent parameters is weaker when the original material contrast is higher. (iii) The results for the smaller contrasts $z \ll 1$ do not follow the same behavior. This may call for the use of alternative iterative schemes, such as the polarization-based formulations, which are known for better accommodating both weak and strong contrasts, see [52].

6.4 Example of a non-linear behavior

Finally, this section investigates the case of a strongly non-linear constitutive relation $\mathscr{C}$ in (1), with the example of a composite exhibiting an incremental elastoplastic behavior at small strains. We consider a flow theory of plasticity, relatively to time $t \in [0, T]$ and governed by the following equations:

$$\begin{cases} \boldsymbol{\sigma}(\boldsymbol{x},t) = \kappa(\boldsymbol{x}) \operatorname{tr}(\boldsymbol{\varepsilon}(\boldsymbol{x},t))\boldsymbol{I} + 2\mu(\boldsymbol{x})\big(\boldsymbol{\varepsilon}^d(\boldsymbol{x},t) - \boldsymbol{\varepsilon}^p(\boldsymbol{x},t)\big), \\ \sigma_{\mathrm{eq}}(\boldsymbol{x},t) - \sigma_0(\boldsymbol{x}) \le 0, \\ \dot{\boldsymbol{\varepsilon}}^p(\boldsymbol{x},t) = \dot{p}(\boldsymbol{x},t)\dfrac{3\boldsymbol{\sigma}^d(\boldsymbol{x},t)}{2\sigma_{\mathrm{eq}}(\boldsymbol{x},t)}, \quad \dot{p}(\boldsymbol{x},t) \ge 0, \quad \dot{p}(\boldsymbol{x},t)\big(\sigma_{\mathrm{eq}}(\boldsymbol{x},t) - \sigma_0(\boldsymbol{x})\big) = 0. \end{cases} \tag{39}$$

The system (39) is written in terms of the strain field $\boldsymbol{\varepsilon} = \frac{1}{2}\big(\operatorname{grad}\boldsymbol{u} + \operatorname{grad}\boldsymbol{u}^T\big)$, its deviatoric counterpart $\boldsymbol{\varepsilon}^d \overset{\text{def}}{=} \boldsymbol{\varepsilon} - \operatorname{tr}(\boldsymbol{\varepsilon})\boldsymbol{I}/3$ and this $\boldsymbol{\sigma}^d$ of the stress tensor, as well as the equivalent stress $\sigma_{\mathrm{eq}} = \big(\frac{3}{2}\boldsymbol{\sigma}^d : \boldsymbol{\sigma}^d\big)^{1/2}$, while $\boldsymbol{\varepsilon}^p$ is the plastic strain and p the cumulated plastic strain. The dot notation refers to the time derivative. The locally-defined material parameters are the yield stress σ_0, and κ, μ the bulk and shear moduli, respectively.

Here, the material is chosen as a set of purely elastic isotropic inclusions embedded in an isotropic elastic and perfectly plastic matrix. It is understood that σ_0 can be taken as infinite in the material phases that are purely elastic. We consider the random circular inclusion case, with the geometry of Figure 3b discretized on a grid with $N = 2^7 + 1$. We define the elasticity moduli in (39) through the Young's modulus E and the Poisson's ratio ν, with $E = 400\,\mathrm{GPa}$ and $\nu = 0.3$ in the elastic inclusions, while $E = 60\,\mathrm{GPa}$, $\nu = 0.2$ and $\sigma_0 = 20\,\mathrm{MPa}$ in the elastoplastic matrix. The unit cell is subjected to an applied macroscopic strain $\boldsymbol{g}_0 = 5 \cdot 10^{-3} \operatorname{diag}(1, -1, 0)$, which is applied gradually over the time interval discretized in 100 steps and (39) is solved using the radial return algorithm, see [44].

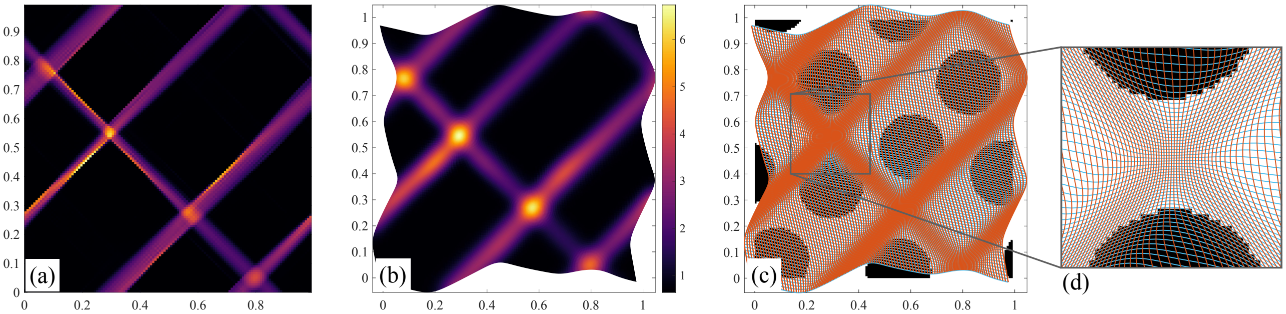

Figure 25: Grid adaptation for the elastoplastic problem in the random circular inclusions case, based on the computation of a preliminary solution $\boldsymbol{u}$: (a) Equivalent strain $\varepsilon_{\mathrm{eq}}(\boldsymbol{x})$, (b) target density function $t(\boldsymbol{x})$, (c) adapted grid (red/blue), (d) close-up.

Grid adaptation. As can be expected with the perfectly plastic behavior in the configuration considered, the deformation tends to localize in the matrix to form slip bands, with angle $\pm\pi/4$ to the direction of the applied traction. To increase the accuracy of the computation, we choose the a posteriori solution-based approach of Section 3.2.2, with a monitor function defined from a preliminary solution computed on a regular grid. More specifically, the target density function $t(\boldsymbol{x})$ is computed from a smoothed and rescaled version $\mathcal{G}[\varepsilon_{\text{eq}}](\boldsymbol{x})$ of the associated equivalent strain field $\varepsilon_{\text{eq}} = \left(\frac{2}{3}\boldsymbol{\varepsilon}^d : \boldsymbol{\varepsilon}^d\right)^{1/2}$. The application of the proposed optimal transport-based Algorithm 1 leads to the results shown in Figure 25, where the regions with a higher density of grid points in Ω_P overlay the slip bands.

Convergence and full-field comparisons. The transported elastoplastic problem (19) is then solved, by applying at each time step, the fixed-point algorithm (36) to compute the full displacement field. Here, we define the stopping criterion as the L^2-norm of the equilibrium equation, with a tolerance set as $\epsilon = 10^{-2}$. A comparison of the equivalent strains computed on the regular and adapted grids is then shown in Figure 26. While these fields agree qualitatively, which validates in the non-linear case the overall approach proposed, the computation performed on the adapted grid is found to be better resolved in the regions of high strains.

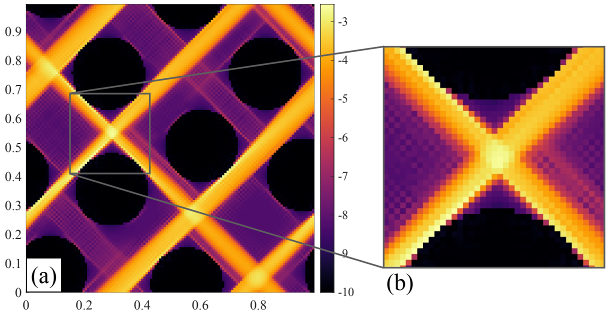

Figure 26: Random circular inclusions in the elastoplastic case: comparison of the equivalent strain $\varepsilon_{\text{eq}}(\boldsymbol{x})$ (in log scale) associated with the solution to (1) with (39) in Ω_P computed using (a) a regular grid and (c) the adapted grid of Fig. 25, with close-ups in (b) and (d), respectively.

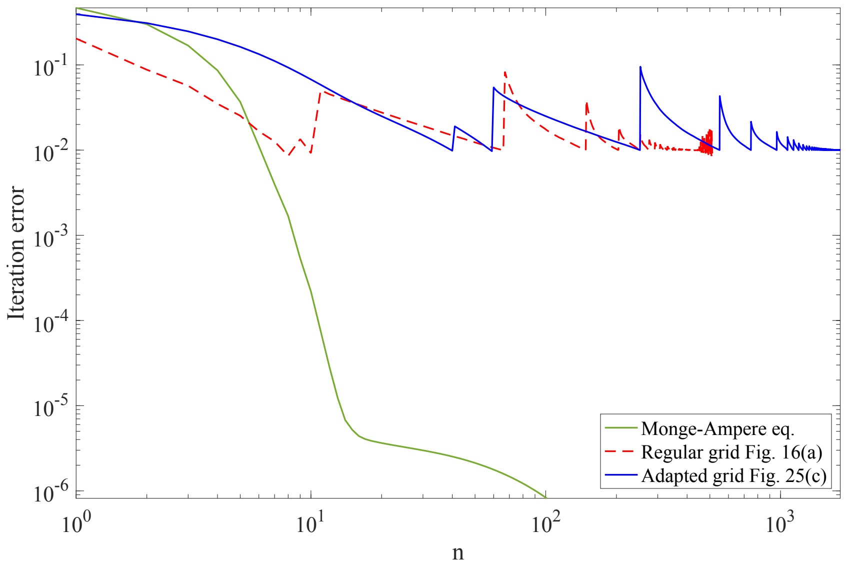

Figure 27: Random circular inclusions in the elastoplastic case: comparison of the iteration errors in solving the PDE considered using a regular grid or the shown adapted grid (see Fig. 25), as functions of the cumulative iteration number n (in log-log scale) for fixed-point iterations. The loading is applied linearly over 100 steps. The corresponding computed fields are shown in Fig. 26.

For a more quantitative analysis, we report in Figure 27 the iteration errors associated with the computations of the solution on a regular grid and on the adapted grid. The numerical cost associated with the resolution of the Monge-Ampère equation using Algorithm 1, with a tolerance set at $\epsilon = 10^{-6}$ as previously, is also included for comparison. First, it can be seen that, in this elastoplastic case, the ratio between the cost for adapting grid and that of computing the solution to the problem at hand itself is more favorable than in the linear case, which argues in favor of including this pre-processing in standard numerical tools. As of the computation of the solution to the transported problem, a larger number of fixed-point iterations is required compared to regular grid computations, since the contrast in the virtual material has increased, as already discussed in the linear case. This drawback can be counterbalanced by using a faster iterative scheme, such as the CG as was done previously or an accelerated gradient-based algorithm, see the review article [52].

	Ref. reg. grid $N = 2^9 + 1$	Reg. grid $N = 2^7 + 1$	Adapt. grid $N = 2^7 + 1$
$\langle \sigma_{11}(\cdot, T)\rangle_{\Omega_P}$ (MPa)	11.5240	11.5358	11.5323
relative error	–	$1.02 \cdot 10^{-3}$	$7.19 \cdot 10^{-4}$
$\langle p(\cdot, T)\rangle_{\Omega_P}$	$5.5894 \cdot 10^{-3}$	$5.5921 \cdot 10^{-3}$	$5.5915 \cdot 10^{-3}$
relative error	–	$4.91 \cdot 10^{-4}$	$3.84 \cdot 10^{-4}$

Table 2: Mean stresses in the direction of the applied loading and global cumulated plastic strains, with errors relative to the first column.

If more iterations are required to achieve convergence using the adapted grid, it nevertheless enables to compute a more accurate approximation of the solution. While a qualitative full-field comparison is exposed in Figure 26, we report in Table 2 the values obtained at convergence of the final mean stress $\langle \sigma_{11}(\cdot, T)\rangle_{\Omega_P}$ in the direction of the applied loading, and of the global cumulated plastic strain $\langle p(\cdot, T)\rangle_{\Omega_P}$. A reference FFT-based solution is computed on a fine regular grid with $N = 2^9 + 1$, all else being equal, to compare the solutions obtained with $N = 2^7 + 1$ on the regular and adapted grids. By comparison with the reference solution, the relative errors show a reduction of about 30% and 22%, respectively, using the adaptive computations. This is consistent with the improvements already observed in the linear cases investigated, which, in the context of this study, constitutes an initial proof of concept. This is all the more valuable in the non-linear case, as increasing the discretization parameter N bears a much higher numerical cost than in the linear case.

7 Conclusion

In this work we have proposed an adaptive Fourier spectral method to perform computations of periodic cell problems on non-uniform grids. This type of problem is central to homogenization schemes but it can also be encountered in different contexts, making our approach possibly relevant in other fields. The key points of this study are the following:

1. A coordinate mapping is introduced as a bijective application between the physical domain, where the original equation is formulated, and the computational domain, where it is intended to be solved numerically. The associated transformation rules are classical, noting in particular the choice made to not apply a gauge transformation to the unknown field itself. This process has some connections with Lagrangian formulations of large-strain elasticity problems, but here the coordinate mapping has no physical meaning.
2. Proper computation of this mapping is then the first key ingredient to the method. While analytical transformations are relevant in some cases (as illustrated), a robust numerical scheme will most often be needed. To this end, we turned to an approach based on optimal transport, to determine a transformation that maps a source density of grid points, likely to be the uniform one in the computational

domain, to a target density, designed to be non-uniform in the physical domain. This amounts to finding the mapping whose Jacobian satisfies a non-linear Monge-Ampère equation.

3. This equation for the mapping is solved using a quasi-Newton method, using tools that are readily available in most FFT-based numerical platforms.

4. A second important aspect of the method is the definition of the target point density, which allows control of the (non-uniform) spatial distribution of grid points in the physical domain. Rather than advocating a specific choice, we chose to investigate a number of options, either on the basis of a priori material-based considerations, or a posteriori using a preliminary solution computed on a non-adapted grid. This illustrates the variety of possibilities for the adaptive process.

5. The original problem is then transported from the physical domain to the computational one. Expressing the latter in divergence form reveals a virtual constitutive relation and some virtual source terms, which combine those in the original equation with the Jacobian matrix of the transformation. As a consequence, the original tensor symmetries are modified, which is analyzed in further details in the linear case.

6. Proper computation of the solution to the transported problem in the computational domain is then addressed, by showing that standard FFT-based schemes on a regular grid are applicable, namely fixed-point iterations or gradient-based algorithms. A minor modification of the Green's tensor must nonetheless be made by using a non-symmetrized version. In addition, the contrast in the virtual constitutive relation would be larger than in the original material, slowing down the convergence of iterative schemes. This drawback can however be compensated by the use of a fast gradient algorithm, a topic that has been the subject of much developments recently.

7. A set of numerical examples are included, illustrating the use of an analytical mapping and the proposed optimal transport-based algorithm. In addition, a variety of monitor functions are explored to adapt the grid to different microstructures. The effect of the grid adaptation is discussed, qualitatively with full-field comparisons of solutions computed on a regular grid or adapted ones, and quantitatively through convergence analyses regarding both the number of iterations, the discretization and the original material contrast. These numerical results show that a systematic gain in precision is achieved using the adaptive method, both in the linear and non-linear cases studied.

To conclude, the proposed adaptive Fourier spectral method can be used to improve the accuracy of a numerical approximation computed on a regular grid, provided that the monitor function is adequately defined. It easily amenable to common FFT-based platforms as it is minimally intrusive: its implementation only necessitates (i) the computation of the Monge-Ampère equation, a problem set in divergence form, (ii) the introduction of the virtual constitutive relation and source terms, and (iii) a minor modification of the Green's tensor.

This study raises a number of questions that could be the subject of future work. First, the choice of the monitor function can be investigated more quantitatively. In particular, the use of a posteriori error estimators seems particularly relevant, see [24]. Second, the transported cell problem features non-fully symmetric tensors, which was not an obstacle for our purposes. Yet, the interest of a fully symmetric formulation could be questioned [41]. Moreover, as the transported problem ultimately solved on a regular grid exhibits larger contrasts compared to the original material, the competing advantages of the various fast gradient methods could be analyzed for this purpose. Quantifying the improvements achieved by the proposed method should also be studied from a numerical analysis standpoint, in particular by understanding the effect of the grid morphing in the Fourier domain. Lastly, it would be interesting to investigate the coupling of the proposed method with other numerical strategies that have shown to globally improve computations on regular FFT grids, such as the composite voxel techniques [26, 32] or the use of modified Green's functions, see e.g. [61].

Acknowledgements: Fruitful discussions with Stéphane Bourgeois, Djaffar Boussaa, Hervé Moulinec and Pierre Suquet are gratefully acknowledged.

A Green's tensor symmetry properties

To compute the periodic gradient Green's operator of Definition 2, the inverse is computed algebraically in Fourier space. The construction of $\widetilde{\boldsymbol{\Gamma}}_0$ from (29) is done through the introduction of the Fourier transform in space, which we denote as $\widehat{\boldsymbol{T}}(\boldsymbol{\xi}) = \mathscr{F}[\boldsymbol{T}](\boldsymbol{\xi})$ for any tensor field $\boldsymbol{T}$, with $\boldsymbol{\xi}$ being the Fourier variable. The cases where $\boldsymbol{C}_0$ is a conductivity or elasticity tensor are examine below.

A.1 Conductivity case

Let us first examine the conductivity case (26). Since the featured virtual constitutive tensor $\widetilde{\boldsymbol{C}}$ is symmetric then we are in a standard case where the second-order Green's tensor is defined in the Fourier domain with components

$$\big(\widehat{\widetilde{\boldsymbol{\Gamma}}}_0(\boldsymbol{\xi})\big)_{ij} = \frac{\xi_i\,\xi_j}{(C_0)_{k\ell}\,\xi_k\,\xi_\ell} \qquad \forall \boldsymbol{\xi} \neq \boldsymbol{0}. \tag{40}$$

Note that one can set $\widehat{\widetilde{\boldsymbol{\Gamma}}}_0(\boldsymbol{0}) = \boldsymbol{0}$ as the iterative schemes is expressed in terms of the gradient of the periodic field U, the former being thus of zero mean. Given (40) then the scheme (31) makes use of

$$\Big(\big[\widetilde{\boldsymbol{\Gamma}}_0\,\widetilde{\boldsymbol{\Sigma}}^{(n)}\big](\boldsymbol{X})\Big)_i = \mathscr{F}^{-1}\Big[\big(\widehat{\widetilde{\Gamma}}_0\big)_{ij}\,\widehat{\widetilde{\Sigma}_j^{(n)}}\Big](\boldsymbol{X}) \quad \text{with} \quad \widetilde{\Sigma}_j^{(n)}(\boldsymbol{X}) = \big(\widetilde{C}(\boldsymbol{X})\big)_{jp}\Big(\big(\widetilde{G}_0(\boldsymbol{X})\big)_p + \frac{\partial U^{(n)}}{\partial X_p}(\boldsymbol{X})\Big).$$

As a consequence, Property 4 holds trivially, i.e. $\big[\widetilde{\boldsymbol{\Gamma}}_0\,\boldsymbol{C}_0\,\mathrm{Grad}\,U\big](\boldsymbol{X}) = \mathrm{Grad}\,U(\boldsymbol{X})$.

A.2 Elasticity case

In the elasticity case, because of the symmetry properties in Corollary 3, the situation is slightly different and the Green's tensor must be adapted accordingly compared to the standard case. Note that what we describe next is similar to the formalism employed for computations at large strains, see [33, 34].

When solving (19) with (27) in the Fourier domain through the introduction of a reference homogeneous tensor $\boldsymbol{C}_0$, with major index symmetry, one arrives at a fourth-order Green's tensor defined with components

$$\big(\widehat{\widetilde{\boldsymbol{\Gamma}}}_0(\boldsymbol{\xi})\big)_{ijk\ell} = \xi_j\big(\boldsymbol{K}_0^{-1}(\boldsymbol{\xi})\big)_{ik}\xi_\ell \qquad \text{with} \qquad \big(\boldsymbol{K}_0(\boldsymbol{\xi})\big)_{ik} = (C_0)_{ipkq}\,\xi_p\,\xi_q \tag{41}$$

for all non-zero spatial frequency $\boldsymbol{\xi}$. Again, one can set $\widehat{\widetilde{\boldsymbol{\Gamma}}}_0(\boldsymbol{0}) = \boldsymbol{0}$.

Property 5. *The second-order tensor $\boldsymbol{K}_0$ defined in (41) is symmetric, hence the associated Green's tensor $\widehat{\widetilde{\boldsymbol{\Gamma}}}_0$ satisfies the following index symmetries:*

$$\big(\widehat{\widetilde{\Gamma}}_0\big)_{ijk\ell} = \big(\widehat{\widetilde{\Gamma}}_0\big)_{kji\ell} = \big(\widehat{\widetilde{\Gamma}}_0\big)_{i\ell kj}.$$

Proof. From the definition (41) and using the major index symmetry of $\boldsymbol{C}_0$ then one has

$$(K_0)_{ik} = (C_0)_{ipkq}\,\xi_p\,\xi_q = (C_0)_{kqip}\,\xi_q\,\xi_p = (K_0)_{ki}.$$

This entails the symmetry of $\big(\widehat{\widetilde{\Gamma}}_0\big)_{ijk\ell}$ on the indices i, k while this on j, ℓ immediately follows from the term $\xi_j\xi_\ell$ in the definition of the former. □

In this context, to make the terms in (31) more explicit, one must note that

$$\Big(\big[\widetilde{\boldsymbol{\Gamma}}_0\,\widetilde{\boldsymbol{\Sigma}}^{(n)}\big](\boldsymbol{X})\Big)_{ij} = \mathscr{F}^{-1}\Big[\big(\widehat{\widetilde{\Gamma}_0}\big)_{ijk\ell}\,\widehat{\widetilde{\Sigma}^{(n)}_{k\ell}}\Big](\boldsymbol{X})$$

$$\text{with}\qquad \widetilde{\Sigma}^{(n)}_{k\ell}(\boldsymbol{X}) = \big(\widetilde{C}(\boldsymbol{X})\big)_{k\ell pq}\Big(\big(\widetilde{G}_0(\boldsymbol{X})\big)_{pq} + \frac{\partial U_p^{(n)}}{\partial X_q}(\boldsymbol{X})\Big).$$

Finally, using the previous identity, one can show that the projection identity (32) also holds in the elasticity case. Indeed, one has

$$\begin{aligned}\Big(\big[\widetilde{\boldsymbol{\Gamma}}_0\,\boldsymbol{C}_0\,\mathrm{Grad}\,\boldsymbol{U}\big](\boldsymbol{X})\Big)_{ij} &= \mathscr{F}^{-1}\Big[\big(\widehat{\widetilde{\Gamma}_0}\big)_{ijk\ell}\,(C_0)_{k\ell pq}\,\mathrm{i}\xi_q\,\widehat{U}_p\Big](\boldsymbol{X})\\ &= \mathscr{F}^{-1}\Big[\xi_j\big(\boldsymbol{K}_0^{-1}(\boldsymbol{\xi})\big)_{ik}\xi_\ell\,(C_0)_{k\ell pq}\,\mathrm{i}\xi_q\,\widehat{U}_p\Big](\boldsymbol{X})\end{aligned}$$

but $\xi_\ell (C_0)_{k\ell pq}\xi_q = \big(\boldsymbol{K}_0(\boldsymbol{\xi})\big)_{kp}$ so that $\big(\boldsymbol{K}_0^{-1}(\boldsymbol{\xi})\big)_{ik}\xi_\ell\,(C_0)_{k\ell pq}\xi_q = \delta_{ip}$. Therefore, we obtain

$$\Big(\big[\widetilde{\boldsymbol{\Gamma}}_0\,\boldsymbol{C}_0\,\mathrm{Grad}\,\boldsymbol{U}\big](\boldsymbol{X})\Big)_{ij} = \mathscr{F}^{-1}\Big[\mathrm{i}\xi_j\,\widehat{U}_i\Big](\boldsymbol{X}) = \frac{\partial U_i}{\partial X_j}(\boldsymbol{X}),$$

which establishes the projection Property 4 in the elasticity case.

References

[1] Cédric Bellis and Pierre Suquet. Geometric variational principles for computational homogenization. *Journal of Elasticity*, 137(2):119–149, 2019.

[2] Cédric Bellis, Hervé Moulinec, and Pierre Suquet. Eigendecomposition-based convergence analysis of the neumann series for laminated composites and discretization error estimation. *International Journal for Numerical Methods in Engineering*, 121(2):201–232, 2020.

[3] Benamou, Jean-David, Froese, Brittany D., and Oberman, Adam M. Two Numerical Methods for the elliptic Monge-Ampère equation. *ESAIM: M2AN*, 44(4):737–758, 2010.

[4] Pavel Bochev, Guojun Liao, and Gary dela Pena. Analysis and computation of adaptive moving grids by deformation. *Numerical Methods for Partial Differential Equations*, 12(4):489–506, 1996.

[5] J. P. Boyd. *Chebyshev and Fourier Spectral Methods.* Dover, New-York, 2000.

[6] John P. Boyd. The Rate of Convergence of Fourier Coefficients for Entire Functions of Infinite Order with Application to the Weideman-Cloot Sinh-Mapping for Pseudospectral Computations on an Infinite Interval. *Journal of Computational Physics*, 110(2):360 – 372, 1994.

[7] Y. Brenier. Polar factorization and monotone rearrangement of vector-valued functions. *Communications on Pure and Applied Mathematics*, 44(4):375–417, 1991.

[8] C. J. Budd and J. F. Williams. Moving Mesh Generation Using the Parabolic Monge–Ampère Equation. *SIAM Journal on Scientific Computing*, 31(5):3438–3465, 2009.

[9] F. Caforio and S. Imperiale. A High-Order Spectral Element Fast Fourier Transform for the Poisson Equation. *SIAM Journal on Scientific Computing*, 41(5):A2747–A2771, 2019.

[10] Weiming Cao, Weizhang Huang, and Robert D. Russell. A study of monitor functions for two-dimensional adaptive mesh generation. *SIAM Journal on Scientific Computing*, 20(6):1978–1994, 1999.

[11] Hector D. Ceniceros and Thomas Y. Hou. An efficient dynamically adaptive mesh for potentially singular solutions. *Journal of Computational Physics*, 172(2):609 – 639, 2001.

[12] P. G. Ciarlet. *The Finite Element Method for Elliptic Problems.* North-Holland, 1978.

[13] P. G. Ciarlet. *Mathematical elasticity, volume I: Three-dimensional elasticity.* North-Holland, 1988.

[14] A. Cloot. Equidistributing mapping and spectral method for the computation on unbounded domains. *Applied Mathematics Letters*, 4(4):23 – 27, 1991.

[15] A Cloot and J.A.C Weideman. An adaptive algorithm for spectral computations on unbounded domains. *Journal of Computational Physics*, 102(2):398 – 406, 1992.

[16] Rémi Cornaggia, Marie Touboul, and Cédric Bellis. FFT-based computation of homogenized interface parameters. *Comptes Rendus. Mécanique*, 350:297–307, 2022.

[17] Rémi Cornaggia and Cédric Bellis. Tuning effective dynamical properties of periodic media by FFT-accelerated topological optimization. *International Journal for Numerical Methods in Engineering*, 121(14):3178–3205, 2020.

[18] E. & F. Cosserat. *Théorie des corps déformables.* Hermann, 1909.

[19] G.L. Delzanno, L. Chacón, J.M. Finn, Y. Chung, and G. Lapenta. An optimal robust equidistribution method for two-dimensional grid adaptation based on Monge–Kantorovich optimization. *Journal of Computational Physics*, 227(23):9841–9864, 2008.

[20] A. Dutt and V. Rokhlin. Fast fourier transforms for nonequispaced data. *SIAM Journal on Scientific Computing*, 14(6):1368–1393, 1993.

[21] Arkady S Dvinsky. Adaptive grid generation from harmonic maps on Riemannian manifolds. *Journal of Computational Physics*, 95(2):450 – 476, 1991.

[22] D. J. Eyre and G. W. Milton. A fast numerical scheme for computing the response of composites using grid refinement. *Eur. Phys. J. Appl. Phys.*, 6:41–47, 1999.

[23] W.M. Feng, P. Yu, S.Y. Hu, Z.K. Liu, Q. Du, and L.Q. Chen. Spectral implementation of an adaptive moving mesh method for phase-field equations. *Journal of Computational Physics*, 220(1):498 – 510, 2006.

[24] Renaud Ferrier and Cédric Bellis. A posteriori error estimations and convergence criteria in fast Fourier transform-based computational homogenization. *International Journal for Numerical Methods in Engineering*, 124(4):834–863, 2023.

[25] Valentin Gallican, Miroslav Zecevic, Ricardo A. Lebensohn, and Martín I. Idiart. The elastic properties of dilute solid suspensions with imperfect interfacial bonding: Variational approximations versus full-field simulations. *Journal of Elasticity*, 153:373–398, 2023.

[26] Lionel Gélébart and Franck Ouaki. Filtering material properties to improve FFT-based methods for numerical homogenization. *Journal of Computational Physics*, 294:90–95, 2015.

[27] W. Huang and R. D. Russell. *Adaptive Moving Mesh Methods.* Springer, 2011.

[28] Weizhang Huang. Practical aspects of formulation and solution of moving mesh partial differential equations. *Journal of Computational Physics*, 171(2):753 – 775, 2001.

[29] Weizhang Huang. Variational mesh adaptation: Isotropy and equidistribution. *Journal of Computational Physics*, 174(2):903 – 924, 2001.

[30] Weizhang Huang, Yuhe Ren, and Robert D. Russell. Moving Mesh Partial Differential Equations (MMPDES) Based on the Equidistribution Principle. *SIAM Journal on Numerical Analysis*, 31(3):709–730, 1994.

[31] M. Kabel, T. Böhlke, and M. Schneider. Efficient fixed point and Newton-Krylov solvers for FFT-based homogenization of elasticity at large deformations. *Comput. Mech.*, 54:1497–1514, 2014.

[32] Matthias Kabel, Dennis Merkert, and Matti Schneider. Use of composite voxels in fft-based homogenization. *Computer Methods in Applied Mechanics and Engineering*, 294:168–188, 2015.

[33] N. Lahellec. *Homogénéisation et étude expérimentale de composites hyperélastiques et visco-hyperélastiques.* PhD thesis, Université Aix-Marseille II, 2001.

[34] N. Lahellec, J.C. Michel, H. Moulinec, and P. Suquet. Analysis of Inhomogeneous Materials at Large Strains using Fast Fourier Transforms. *IUTAM Symposium on Computational Mechanics of Solid Materials at Large Strains. Solid Mechanics and Its Applications*, 108, 2003.

[35] Grégoire Loeper and Francesca Rapetti. Numerical solution of the Monge–Ampère equation by a Newton's algorithm. *Comptes Rendus Mathematique*, 340(4):319–324, 2005.

[36] John Maclean, J. E. Bunder, I. G. Kevrekidis, and A. J. Roberts. Adaptively detect and accurately resolve macro-scale shocks in an efficient equation-free multiscale simulation. *SIAM Journal on Scientific Computing*, 44(4):A2557–A2581, 2022.

[37] Jean-Jacques Marigo, Agnès Maurel, Kim Pham, and Amine Sbitti. Effective dynamic properties of a row of elastic inclusions: The case of scalar shear waves. *Journal of Elasticity*, 128(2):265–289, 2017.

[38] Andrew T. T. McRae, Colin J. Cotter, and Chris J. Budd. Optimal-transport–based mesh adaptivity on the plane and sphere using finite elements. *SIAM Journal on Scientific Computing*, 40(2):A1121–A1148, 2018.

[39] Morteza M. Mehrabadi and Stephen C. Cowin. Eigentensors of linear anisotropic elastic materials. *The Quarterly Journal of Mechanics and Applied Mathematics*, 43(1):15–41, 1990.

[40] G. W. Milton. *The Theory of Composites.* Cambridge university press, 2002.

[41] Graeme W Milton, Marc Briane, and John R Willis. On cloaking for elasticity and physical equations with a transformation invariant form. *New Journal of Physics*, 8(10):248, oct 2006.

[42] H. Moulinec. Private communication.

[43] H. Moulinec and P. Suquet. A fast numerical method for computing the linear and nonlinear properties of composites. *C. R. Acad. Sc. Paris, II*, 318:1417–1423, 1994.

[44] H. Moulinec and P. Suquet. A numerical method for computing the overall response of nonlinear composites with complex microstructure. *Comp. Meth. Appl. Mech. Engng.*, 157:69–94, 1998.

[45] L. S. Mulholland, W. Z. Huang, and D. M. Sloan. Pseudospectral solution of near-singular problems using numerical coordinate transformations based on adaptivity. *SIAM Journal on Scientific Computing*, 19(4):1261–1289, 1998.

[46] Noé Brice Nkoumbou Kaptchouang and Lionel Gélébart. Multiscale coupling of FFT-based simulations with the LDC approach. *Computer Methods in Applied Mechanics and Engineering*, 394:114921, 2022.

[47] A.N. Norris and A.L. Shuvalov. Elastic cloaking theory. *Wave Motion*, 48(6):525–538, 2011. Special Issue on Cloaking of Wave Motion.

[48] Y. V. Obnosov. Periodic heterogeneous structures: new explicit solutions and effective characteristics of refraction of an imposed field. *SIAM J Appl Math.*, 59(4):1267–1287, 1999.

[49] E Sanchez-Palencia. *Non-Homogeneous Media and Vibration Theory.* Springer, Berlin, Heidelberg, 1978.

[50] Filippo Santambrogio. *Optimal Transport for Applied Mathematicians.* Birkhäuser, 2015.

[51] Louis-Philippe Saumier, Martial Agueh, and Boualem Khouider. An efficient numerical algorithm for the L2 optimal transport problem with periodic densities. *IMA Journal of Applied Mathematics*, 80(1):135–157, 06 2013.

[52] Matti Schneider. A review of nonlinear FFT-based computational homogenization methods. *Acta Mechanica*, 232(6):2051–2100, 2021.

[53] Matti Schneider. On the effectiveness of the Moulinec–Suquet discretization for composite materials. *International Journal for Numerical Methods in Engineering*, 124(14):3191–3218, 2023.

[54] Jie Shen and Xiaofeng Yang. An efficient moving mesh spectral method for the phase-field model of two-phase flows. *Journal of Computational Physics*, 228(8):2978 – 2992, 2009.

[55] Mohamed Sulman, J.F. Williams, and R.D. Russell. Optimal mass transport for higher dimensional adaptive grid generation. *Journal of Computational Physics*, 230(9):3302–3330, 2011.

[56] M. Touboul. *Acoustic and elastic wave propagation in microstructured media with interfaces: homogenization, simulation and optimization.* PhD thesis, Aix-Marseille Université, 2021.

[57] Marie Touboul, Kim Pham, Agnès Maurel, Jean-Jacques Marigo, Bruno Lombard, and Cédric Bellis. Effective resonant model and simulations in the time-domain of wave scattering from a periodic row of highly-contrasted inclusions. *Journal of Elasticity*, 142(1):53–82, 2020.

[58] J.A.C. Weideman and A. Cloot. Spectral methods and mappings for evolution equations on the infinite line. *Computer Methods in Applied Mechanics and Engineering*, 80(1):467 – 481, 1990.

[59] Hilary Weller, Philip Browne, Chris Budd, and Mike Cullen. Mesh adaptation on the sphere using optimal transport and the numerical solution of a Monge–Ampère type equation. *Journal of Computational Physics*, 308:102–123, 2016.

[60] Daniel Wicht, Matti Schneider, and Thomas Böhlke. On quasi-Newton methods in fast Fourier transform-based micromechanics. *International Journal for Numerical Methods in Engineering*, 121(8):1665–1694, 2020.

[61] F. Willot. Fourier-based schemes for computing the mechanical response of composites with accurate local fields. *Comptes Rendus Mécanique*, 343:232–245, 2015.

[62] Alan M Winslow. Numerical solution of the quasilinear poisson equation in a nonuniform triangle mesh. *Journal of Computational Physics*, 1(2):149 – 172, 1966.

[63] Hiroe Yamazaki, Hilary Weller, Colin J. Cotter, and Philip A. Browne. Conservation with moving meshes over orography. *Journal of Computational Physics*, 461:111217, 2022.

[64] C. Ye and E.T. Chung. Convergence of trigonometric and finite-difference discretization schemes for FFT-based computational micromechanics. *BIT Numer. Math.*, 63:11, 2023.

[65] P. Yu, L. Q. Chen, and Q. Du. *Applications of Moving Mesh Methods to the Fourier Spectral Approximations of Phase-Field Equations*, pages 80–99. World Scientific, 2008.

[66] Miroslav Zecevic, Ricardo A. Lebensohn, and Laurent Capolungo. New large-strain FFT-based formulation and its application to model strain localization in nano-metallic laminates and other strongly anisotropic crystalline materials. *Mechanics of Materials*, 166:104208, 2022.

[67] Miroslav Zecevic, Ricardo A. Lebensohn, and Laurent Capolungo. Non-local large-strain FFT-based formulation and its application to interface-dominated plasticity of nano-metallic laminates. *Journal of the Mechanics and Physics of Solids*, 173:105187, 2023.